UNIVERSITY OF CALIFORNIA, MERCED

Understanding the Electrochemical Properties of Noble Metal Nanoparticles through Galvanic Equilibration

A dissertation submitted in partial satisfaction of the requirements

for the degree Doctor of Philosophy

in

Chemistry

by

Randy Espinoza

Committee in charge:

Professor Anne Kelley, Chair

Professor Son C. Nguyen

Professor Erik Menke

Professor Sayantani Ghosh

The Dissertation of Randy Espinoza is approved, and it is acceptable in quality and form for publication on microfilm and electronically:

Son C. Nguyen (advisor)	Date
Erik Menke	Date
Sayantani Ghosh	Date
Anne M. Kelley (chair)	Date

University of California, Merced

2023

Table of Contents

List of Figures

List of Tables

Dedication Page

I dedicate this work to my parents who have supported me through this journey all the way.

Dedico este trabajo a mis padres que me han apoyado a lo largo de este viaje y a todos mis amigos y familiares.

Mamá, gracias por apoyarme en este largo y difícil camino. Eh causado muchos dolores de cabeza y te hice preocuparte durante muchas veces. Quería compensar por mis errores en eligiendo esta carrera y espero haberte hecho sentir orgullosa.

Héctor, aunque llegaste más tarde en nuestra vida, te agradezco por apoyando a mi mama, mis hermanos y yo en momentos difíciles en nuestra vida. Muchas gracias porque sin tu ayuda, no sé si lograría estar aquí.

To the rest of my family and friends, thank you for your support and encouragement. This wouldn’t have been possible without you.

Acknowledgements Page

First, I would like to thank my advisor Professor Son Nguyen for supporting me through this long journey and appreciate his many discussions, lessons, advice, and guidance given to me over the years. Although many of our ideas were not fruitful, the successful ideas in this body of work (Chapters 2 and 3) are his and I would like to credit him for that.

I also appreciate my colleagues including Duy Nguyen, Pin Lyu, Daniel V. Cahua, and Ziliang Mao for the awesome discussions, debates, and comradery. I also would like to extend my gratitude to all the undergraduates who have assisted me with my work including Kyle Magro, Anthony Garcia, Adrian Enwright, Sydney Vang, and Riley Whitmer.

I'd also like to thank my committee, including Professors Anne Kelley, Erik Menke, and Sayantani Ghosh for all their advice and guidance and for supporting me through the difficult times.

Finally, I'd like to thank the School of Natural Sciences and the Chemistry and Biochemistry department for providing financial support in form of teaching appointments, graduate student fellowships, and travel grants.

Curriculum Vita, Publications, and Field of Study

Randy Espinoza
Email: randysykesiv@gmail.com | Phone: (559) 301-5157 | 45 Silverhorn Apt 7, Merced, CA 95348

Education

University of California, Merced August 2018 – May 2023 Chemistry, Ph.D. Candidate
Advisor: Prof. Son C. Nguyen

California State University, Fresno August 2015- December 2017
Chemistry, M.S.
Advisor: Prof. Jai-Pil Choi

California State University, Fresno
August 2010 – May 2015
Chemistry, B.A.

Research Background

University of California, Merced
Subject: Redox and photocatalytic properties of noble metal nanoparticles for catalysis

Project 1 - Size-dependent electrochemical properties of colloidal gold nanoparticles

Project 2 - Reduction potentials of gold nanoparticles excited by light

Project 3 - Photocatalysis with non-noble metal nanoparticles

California State University, Fresno

Thesis Project: Investigated electrochemical properties of Au_{25} nanoclusters for sensing applications

Publications

1. Randy Espinoza, Daniel V. Cahua, Kyle Magro, Pin Lyu, Son C. Nguyen, The Nernst equation at the nanoscale: probing the size and surfactant effects on the AuNP reduction potentials, 2023, (In preparation)
2. Pin Lyu, Randy Espinoza, Son C. Nguyen*. Photocatalysis of Metallic Nanoparticles: Interband vs.Plasmon. 2023, In preparation. (Invited review for Nanoscale Advances).

3. Mao, Z.; Espinoza, R.; Garcia, A.; Enwright, A.; Vang, H.; Nguyen, S. C., Tuning Redox Potential of Gold Nanoparticle Photocatalysts by Light. ACS Nano 2020, 14 (6), 7038-7045.
4. Lyu, P.; Espinoza, R.; Khan, M. I.; Spaller, W. C.; Ghosh, S.; Nguyen, S. C., Mechanistic insight into deep holes from interband transitions in Palladium nanoparticle photocatalysts. iScience 2022, 25 (2), 103737.

Mentor and Teaching Roles

Graduate Students

Mentees: Daniel V. Cahua, Jobaer Abdullah, Victor D. Arroyo, and Himani Ahuja at UC Merced

Role: Provided first-year graduate students advice and guidance on navigating through the graduate program

Support: Grad Peer Mentoring Program

Undergraduate Students

Mentees: Riley Whitmer, Denys Chaus, Dylan Yost-Slinker, Kyle Magro, Paulina Brambila, Adrian Enwright, Anthony Garcia, and Hnubci S. Vang

Roles: Guide, instruct and assist students, many of whom were from underrepresented groups in STEM, in reaching their research objectives and instilling core research methods and principles

Support: Learning Aligned Employment Program (LAEP), Merced nAnomaterials Center for Energy and Sensing (MACES), and Undergraduate Research Opportunities Center (UROC)

High School Students

Mentees: Siena Akira Murillo and Ixchel Gonzales

Role: Provide high hands-on experience in *bona fide* research labs

Support: ACS Project seed (formaly "Summer Experiences for the Economically Disadvantaged")

Teaching Assistant

Courses and Labs: general chemistry I and II, physical chemistry, instrumental analysis, and some inorganic chemistry (+7 years)

Skills

Software

Most Windows Office software, OriginLab, ImageJ, Chemdraw, MNova, CrystalMaker

Technical Instrumentation

Well-versed in spectroscopies including UV-Visible, TEM, SEM, DLS/Zeta, Fluorescence, FTIR, NMR, and XPS, with some experience in S/TEM, GC and ICP-OES/MS

Work Experience

California State University, Fresno January 2018 - August 2018
Instructional Support Technician I
Teaching labs and chemical stockroom management and safety

Agriculture and Priority Pollutants Labs, Inc. May 2014 – Aug 2016
Chemical Analyst I
Analysis of agriculturally important heavy metals dissolved in water and soils (non-research)

Awards

MACES summer Fellowship award
2020
University of California, Merced

CCB Summer Fellowship Award
2019
University of California, Merced

B2D scholarship
2016
California State University, Fresno

Conferences, Meetings, and Presentations

- **ACS Spring Meeting**
  2023
- **ARCS foundation**
  2023
- **UCM LAEPs Flash talk**
  2022
- **Molecular Foundry**
  2020
- **UCM Research Week**
  2020

Abstract of the Dissertation

Title: Understanding the Electrochemical Properties of Noble Metal Nanoparticles Through Galvanic Equilibration

Name: Randy Espinoza

Degree: Doctor of Philosophy

Institution: University of California, Merced,

Committee Chair: Anne M. Kelley

Metallic nanoparticles have tunable electrochemical properties that make them suitable for catalyzing redox reactions. Thus, understanding how their reduction potentials respond to changes in particle size and light excitation is important for predicting their chemical stability and catalytic activity. However, establishing their standard reduction potentials through voltammetry has been met with technical challenges, specifically those introduced by the support. To get around this issue, an alternative approach based on Galvanic equilibration was adapted to determine the standard reduction potentials of colloidal NPs, thus avoiding the substrate effects associated with the support. This approach opens the door to exploring various factors that cause the nanoparticle reduction potentials to shift. Factors such as light absorption, changes in particle size, and local environmental effects will be discussed using theoretical models and experimental evidence to help us understand the magnitude of their impacts. Lastly, this approach can be adapted to investigate other factors important to catalysis, including crystallographic shape and atomic arrangement at the surface.

First, Chapter 1 provides a historical context of metallic nanoparticles, from their early uses in decorative artifacts to modern chemical catalysis. Their early uses in art pieces stemmed from their unique optical properties. These optical properties were later determined to result from localized surface plasmon resonance, which became the foundation of metal nanoparticle-driven photocatalysis. Improvements in synthetic and characterization methods made it possible to study in depth their optical, catalytic, and chemical and physical properties concerning particle size. Their electrochemical properties are especially important for understanding their chemical stability and catalytic activity. With great success, such properties have been quantified for substrate-supported metallic nanoparticles through electrochemical methods such as anodic stripping voltammetry. Towards the end of the chapter, we discuss the limitations of voltammetry and how a galvanic equilibration approach can address such issues.

Chapter 2 explains the principles behind the Galvanic equilibration approach in greater detail. This approach allows measuring the standard reduction potentials of spherical AuNPs freely suspended in solution to better understand how they respond to a change in size and the stabilizer ligands without the influence of the substrate supports. As the NPs decrease in size, their reduction potentials shift towards negative values that can be observed by a shift in their equilibrium constant when coupled to a redox probe.

Furthermore, the ligand stabilizers such as quaternary ammonium surfactants are shown to also influence the reduction potentials. These surfactants participate in the redox reactions by interacting with the gold complexes formed during Galvanic equilibration. As a result, surfactants like CTAB significantly lower the standard reduction potentials of the gold nanoparticles, making them more electrochemically reactive. At the end of this chapter, the advantages of using the galvanic equilibration method for measuring the reduction potentials are summarized, and an outlook is given.

Chapter 3 then takes the galvanic equilibration approach to investigate how light absorption induces a shift in the reduction potential. When metallic nanoparticles absorb light, they generate high-energy (hot) electrons and holes (carriers) that can be used to drive chemical transformations on the surface. The efficiency and selectivity of these chemical transformations can be tuned by parameters such as photon flux and energy. For noble metal nanoparticles, how carrier generation is also dependent on the mode of excitation, which include interband and localized surface plasmon resonance. For instance, exciting the NPs at the localized surface plasmon resonance region generates hot electrons relative to the hot holes. On the other hand, exciting at the interband region of AuNPs generates very hot holes relative to the hot electrons. By exciting at the interband region, for example, we can use the high-energy hot holes to catalyze the main oxidation reactions while scavenging the “warmer” electrons using sacrificial compounds. This process can also induce photocharging by selectively harvesting the hot holes and allowing the hot electrons to relax to the ground state and accumulate in the nanoparticle. This photocharging process raises the NP's Fermi level, which can be measured through Galvanic equilibration. The results show that shorter excitation wavelengths induce the largest photocharging and shift the reduction potentials more negatively than longer wavelengths. This observation implies that catalytic activity in metallic nanoparticles can be tuned by light, especially for redox transformations.

Finally, Chapter 4 summarizes the work presented in this dissertation and discusses how galvanic equilibration can be used to study other physical and chemical phenomena, such as the shape effects on the electrochemical properties of NPs. For crystalline nanoparticles, different shapes are dominated by one or more kinds of facets with different surface tension. Because the surface Gibbs free energy depends on the surface tension, their electrochemical properties should vary amongst nanoparticles dominated by different facets. Thus, along with excitation wavelength, size, and stabilizer ligands, the NP shape can also be used to tune metallic NPs’ electrochemical stability and catalytic activity.

Ch. 1 - Introduction to the optical and electrochemical properties of metallic nanoparticles and their catalytic applications

Overview of the properties, applications, and historical context of metallic nanoparticles

The ability of metals to accept and donate electrons critically depends on their redox potential. Recently, this property has allowed noble metal nanoparticles (NPs) to emerge as attractive candidates for catalyzing oxidation and reduction reactions.[1, 2] Furthermore, their ability to harness light energy to drive such chemical transformations, along with their large surface-to-area ratio, corrosion resistance, and unique optical properties, have made them suitable research models in photocatalysts.[3] Therefore, having a fundamental understanding of their physical and chemical properties and how they change at the nanoscale enables the opportunity for developing sustainable catalysts. Their electrochemical properties are especially important since they are subject to changes in NP physical dimensions,[4] electronic states,[5] and chemical environment,[6] and are best evaluated by their reduction potentials. Historically, their reduction potentials have been studied by powerful and robust techniques such as anodic stripping voltammetry.[7] However, such techniques have been met with several challenges due to the inherent nature of the measurement itself. In this body of work, we demonstrate as a proof of concept an electrodeless method for measuring the reduction potentials of colloidal NPs and investigate how their electrochemical properties respond to changes in NP dimensions, local chemical environment, and electronic state.

The use of noble metal NPs dates to ancient Roman times with the famous Lycurgus cup. This ancient artifact contained trace gold and silver metals whose unique optical properties gave it a dichromic appearance.[8] Depending on the observer's position relative to the light source, the Lycurgus cup can appear lustrous ruby red or an opaque olive color, a unique property to noble metal nanoparticles. However, gold and silver in the form of NPs were not known to be the reason for such interesting optical properties. The advancement of characterization techniques, such as the development of the electron microscope, revealed such mysteries.[9, 10] Today, a large body of work is conveniently performed on nanoparticles suspended in aqueous and organic solutions (colloids) rather than in glass.

Nanoparticle synthesis

One of the oldest and simplest methods for synthesizing NPs is the Turkevich method.[11] Briefly, the Turkevich method is based on the reduction of metal precursors with boiling trisodium citrate solutions to generate pseudo-spherical NPs. The simplicity of this method has made it the most common and arguably the most popular way of synthesizing noble metal NPs and, over the years, has been refined to yield better control over particle size distribution and uniformity.[12] More recent synthetic methods utilize a seed-mediated approach to grow NPs of different shapes with precise control over size distributions, excellent uniformity, and better colloidal stability than citrate-stabilized NPs.[13]

NP stability in solution is governed by the protecting capping ligands adsorbed on the surface. These protective adsorbates keep nanoparticles apart by overcoming the attractive Van der Waal forces through steric or electrostatic repulsion.[14] Steric repulsion

typically relies on the bulky nature of the capping agent, which physically prevents the nanoparticles from coalescing or aggregating with one another. This stabilization is typically achieved with large macromolecules such as polymers and bioorganic molecules. Electrostatic stabilization, on the other hand, relies surface charge on the metal nanoparticles to repel one another. This can be achieved by the adsorption of charged molecules on the surfaces. A greater charge density typically provides better stabilizations.

Furthermore, NPs can be stabilized by combining both steric and electrostatic repulsion to achieve greater stabilization. However, there are some ligands that, although they provide excellent stability, may deactivate the surface and render the NP unsuitable for catalytic applications. Thus, a balance between colloidal stability and chemical activity must be achieved for catalytic applications.

Applications in catalysis

A NP's catalytic efficiency depends on various factors, including the NP's size,[15] elemental composition,[1] shape,[16] and the adsorbed ligands.[14] Bare NPs offer the best catalytic activity, however, are not colloidally stable and must be supported on some substrate. NPs stabilized with loosely absorbed or labile ligands offer greater catalytic activity due to a larger availability of active sites for chemical transformations but can often fail at keeping the NP from aggregation after repeated uses. Stronger binding ligands offer a more significant degree of protection against the harsh reaction conditions during catalysis, however, they may counterintuitively block the active sites and poison the catalysts.[14] Thus, one must strike a delicate balance between catalytic efficiency and stabilization by selecting the appropriate ligand or combination of ligands in designing NP catalysts.

More recently, noble metal NPs have shown interesting photocatalytic properties. Noble metals like AuNPs exhibit large optical cross-sections within the visible electromagnetic spectrum. Their large optical cross-sections arise from a combination of interband and localized surface plasmon resonance (LSPR) excitations.[17] LSPR is the oscillations of conduction electrons at the NP surface with a resonant photon. At the same time, interband transitions involve the direct electronic excitation of the electrons in the *d*- to *sp*- band.[18] Bear in mind that most transition metals exhibit these optical properties. These metals often have LSPRs that appear in the UV region with interband excitations spanning broadly across the electromagnetic spectrum.[19, 20] Other than noble metals (Cu, Ag, and Au), few metals like Na exhibit an LSPR in the visible spectrum. Furthermore, the excited electrons generated from light absorption can be harnessed for catalyzing many chemical transformations.[21]

Many photocatalytic reactions are driven by high-energy hot carriers, and many more are being discovered.[3] Excitation at the LSPR or interband regions generates hot carriers that diffuse to the surface to catalyze chemical transformations. Depending on the mode of excitation, the energy associated with hot carriers varies below and above the Fermi level ($E_{F-\hbar\omega}$ and $E_{F+\hbar\omega}$, respectively). For LSPR, electrons are excited to energy levels distributed well above the Fermi level while the hot holes are excited to near the

Fermi level. On the other hand, for interband excitations, the hot holes reside deep within the d-band (far below the Fermi level) while the hot electrons are excited close to the Fermi level.[20] In either case, their lifetimes are short, in the order of picoseconds, and are a bottle neck for improving catalytic efficiency.

The hot carrier lifetimes in metals are short but vary with excitation wavelengths. In AuNPs, for example, the interband hot carrier time constants range from 100 fs for e^-/e^- (electron), 1.7 ps for e^-/phonon (ph), and 90 ps for ph-ph scattering. For LSPR hot carriers, the time constants range from 500 fs e^-/e^-, 2-4 ps e^-/ph, and 100 ps for ph/ph scattering.[18] These short lifetimes translate to short hot-carrier mean free paths in the order of a few tens of nanometers. For example, at 2 eV, Au's mean free path is about 10 nm.[22] Thus, the size of the NP is an important factor in photocatalysis. Large NPs typically suffer from lower photocatalytic efficiency due to the longer lengths the hot carriers must diffuse through.[23] However, these catalytic bottlenecks can be mitigated through other means, such as photocharging.

Under certain circumstances, the hot carriers can be separated to allow the electrons to relax and accumulate in the NP. The accumulation of electrons after light excitation is known as photocharging and can be used to tune their Fermi level, reduction potential, and catalytic activity. Photocharging can be accomplished by selectively quenching the hot holes using a sacrificial molecule to allow the hot electron to decay to the ground state.[24] For interband excitations, the strongly oxidizing deep holes are easily quenched by many organic molecules or the metal NP before recombining with the hot electrons. After several cycles, the accumulated electrons raise the Fermi level, lowering their reduction potentials. In other words, photocharged NPs are chemically more reactive and are considered stronger reductants than uncharged NPs.[5]

Electrochemical properties and stability

In the absence of light, the redox properties of NPs are governed largely by their physical dimensions. Early radiolysis studies involving Ag clusters revealed reduction potentials significantly more negative than the bulk potential. In an extreme example, a single silver atom in solution was estimated to have a standard reduction potential of -1.7 V, enough to reduce a variety of halogenated organic molecules. Aggregations of these silver atoms yielding Ag_n clusters also displayed strong reducing capabilities, though their reactivity decreased with increasing cluster size.[25] Through a thermodynamic approach, Plieth derived equation (1) to relate the size (r) and standard reduction potentials of NPs, E°_{NP}, based on the differences in free Gibbs energy associated with a change in surface area.[4] This model estimates the reduction potentials based on the size of spherical particles. Note that Plieth's equation approximates the reduction potentials of neutral NPs and does not factor in excess charge density, which NPs often carry.

$$E^\circ_{NP} = E^\circ_{Bulk} - \frac{2\gamma V_m}{zF}\frac{1}{r}$$

Charge density in the NP, whether electronic or electrostatic, contributes to the overall standard reduction potential.[26] Charging the NPs can be accomplished through

several methods. For example, strong nucleophiles such as CN and Br- adsorbed at the surface donate negative charge density through their lone pair of electrons. This excess charge density raises the Fermi level but is limited by the maximum surface coverage.[6] Similarly, strong reducing agents inject electrons into the NP and raise their Fermi. These included the reducing agents used during the synthesis; therefore, most NPs carry an excess charge. However, storage of large numbers of excess charge is temporary and is dependent on the NP's capacitance. Over time, the NPs slowly discharge until equilibrated with the environment. The change in charge density is observable as a shift in the LSPR through UV-Vis spectroscopy and can be used for estimating excess charge.[27]

Electrochemical methods for measuring the redox potentials in metallic nanoparticles

To date, voltammetry is the most commonly used method for measuring the electrochemical properties of NPs.[7] Early measurements relied on scanning electron microscopy techniques to measure the electrochemical stability of small metallic clusters supported on a substrate. Initial evidence contradicted Plieth's equation as shown with Cu clusters on Au(111) surfaces.[28] The electrochemical stability of small Cu clusters on Au(111) substrates was 50 – 60 mV greater than the bulk Cu potential. The high stability against dissolution was attributed to quantum effects. However, later studies disputed this interpretation and attributed the high stability to alloying between the clusters and substrate.[29] Later on, voltammetry demonstrated the ability to measure the reduction potentials of NPs electrochemically deposited on the working electrode. Through stripping voltammetry, the AgNP oxidation potentials were shown to be more negative than the bulk due to the size-dependent diffusion profiles of the oxidation products. Still, they were not directly attributed the shifts in potentials to size.[30] Future anodic stripping voltammetry (ASV) measurements disputed these conclusions and demonstrated a size-dependent trend in the oxidation potentials of electrode-supported AgNP, AuNPs, PtNPs, and PdNPs.[31-34] Since then, ASV has been demonstrated to be a powerful tool for measuring the electrochemical properties and behavior of NPs. However, the substrate effects introduced by the electrode support influence their electrochemical behavior and mitigating such effects is a current challenge in voltammetry.

The reduction potential of NPs shifts upon contact with active support. According to Brainina and coworkers, the magnitude of this shift is proportional to the differences in the surface Gibbs free energy associated with the bare NP and the Gibbs free energy of the NP-substrate interactions, which is related to the difference in work function.[35] Generally, a larger difference in work function leads to a greater shift in the potential. Recall that alloying with the NP may also contribute to the overall shift in potential for metal supports. These substrate effects can be minimized to a certain extent by attachment with a molecular linker. However, electrostatic attachment of the NPs onto the electrode leads to a negative shift in the potential. The shifts in potential due to electrostatic charge are quite large by as much as 155 mV compared to AuNPs without electrostatic attachment. Furthermore, this electrostatic effect is most pronounced on the large NPs but diminishes with smaller diameters for poorly understood reasons.[36] Thus,

obtaining an accurate standard reduction potential for metallic NPs through voltammetry remains a technical challenge.

Measuring the reduction potentials in a colloidal state is an alternative approach to overcoming the challenges presented through voltammetry. Such measurement is possible through the Galvanic equilibration between the NPs and a redox couple. In a galvanic reaction, electrons are exchanged between the NP and a redox species in the solution. This is driven by the positive difference in the reduction potential of the two half-reactions in the electrochemical cell. If the reduction potential of NPs is more negative than an oxidizer, they will undergo oxidative etching. However, in the presence of metal precursors (M^+), the NPs will undergo reductive growth if their potentials are more positive than the reducing agent. By allowing these reactions to reach equilibrium, their redox properties can be probed because at equilibrium, the cell potential of the reaction is zero, and according to the Nernst equation, the equilibrium constant of the reaction is related to the standard cell potential. Assuming the standard reduction potential of the redox couple is known, the standard reduction potential NPs can be calculated from the standard cell potential. The advantage of this approach is that the NP colloidal integrity is preserved as the standard reduction potentials are probed without the influence of a substrate.

Probing the NPs through the galvanic equilibration approach also allows measuring the redox potential of colloidal NPs under excitation and as a function of size. Because the NPs are maintained in a dispersed state, their extinction profile can be easily tracked throughout the reactions. This makes measuring their broad optical absorbance with standard spectrophotometric techniques practical for determining the standard reduction potentials under excitation wavelength and the power of incident light. The standard potentials of NPs under a photostationary state have not been measured by voltammetry.

Dissertation summary

In this dissertation, the following topics are covered in the chapters composing the body of this document: the optical properties of AuNPs, including LSPR and interband absorbance, hot-carrier mechanisms, hot carrier applications in photocatalysis, seed-mediated synthesis of the AuNPs, galvanic equilibration under a photostationary state, the Nernst's equation at the nanoscale, photocharging mechanisms, and the AuNP reduction potentials under photoexcitation, as a function of size, and in micellar media. The conclusion will summarize this body of work, provide fundamental insights into the electrochemical properties of solid-state materials at the nanoscale, and suggest future outlook.

Ch. 1 Reference

(1) Shi, Y.; Lyu, Z.; Zhao, M.; Chen, R.; Nguyen, Q. N.; Xia, Y. Noble-Metal Nanocrystals with Controlled Shapes for Catalytic and Electrocatalytic Applications. *Chemical Reviews* **2020**. DOI: 10.1021/acs.chemrev.0c00454.
(2) Liu, L.; Corma, A. Metal Catalysts for Heterogeneous Catalysis: From Single Atoms to Nanoclusters and Nanoparticles. *Chemical Reviews* **2018**, *118* (10), 4981-5079. DOI: 10.1021/acs.chemrev.7b00776.
(3) Gellé, A.; Jin, T.; de la Garza, L.; Price, G. D.; Besteiro, L. V.; Moores, A. Applications of Plasmon-Enhanced Nanocatalysis to Organic Transformations. *Chemical Reviews* **2020**, *120* (2), 986-1041. DOI: 10.1021/acs.chemrev.9b00187.
(4) Plieth, W. J. Electrochemical properties of small clusters of metal atoms and their role in the surface enhanced Raman scattering. *The Journal of Physical Chemistry* **1982**, *86* (16), 3166-3170. DOI: 10.1021/j100213a020.
(5) Mao, Z.; Espinoza, R.; Garcia, A.; Enwright, A.; Vang, H.; Nguyen, S. C. Tuning Redox Potential of Gold Nanoparticle Photocatalysts by Light. *ACS Nano* **2020**, *14* (6), 7038-7045. DOI: 10.1021/acsnano.0c01704.
(6) Mulvaney, P.; Linnert, T.; Henglein, A. Surface chemistry of colloidal silver in aqueous solution: observations on chemisorption and reactivity. *The Journal of Physical Chemistry* **1991**, *95* (20), 7843-7846. DOI: 10.1021/j100173a053.
(7) Pattadar, D. K.; Sharma, J. N.; Mainali, B. P.; Zamborini, F. P. Anodic stripping electrochemical analysis of metal nanoparticles. *Current Opinion in Electrochemistry* **2019**, *13*, 147-156. DOI: https://doi.org/10.1016/j.coelec.2018.12.006.
(8) Marzinzik, S. *Masterpieces: Early Medieval Art*; British Museum Press, 2013.
(9) Faraday, M. The Bakerian Lecture: Experimental Relations of Gold (and Other Metals) to Light. *Philosophical Transactions of the Royal Society of London* **1857**, *147*, 145-181.
(10) Turkevich, J.; Hillier, J. Electron Microscopy of Colloidal Systems. *Analytical Chemistry* **1949**, *21* (4), 475-485. DOI: 10.1021/ac60028a009.
(11) Turkevich, J.; Stevenson, P. C.; Hillier, J. A study of the nucleation and growth processes in the synthesis of colloidal gold. *Discussions of the Faraday Society* **1951**, *11* (0), 55-75, 10.1039/DF9511100055. DOI: 10.1039/DF9511100055.
(12) Wuithschick, M.; Birnbaum, A.; Witte, S.; Sztucki, M.; Vainio, U.; Pinna, N.; Rademann, K.; Emmerling, F.; Kraehnert, R.; Polte, J. Turkevich in New Robes: Key Questions Answered for the Most Common Gold Nanoparticle Synthesis. *ACS Nano* **2015**, *9* (7), 7052-7071. DOI: 10.1021/acsnano.5b01579.
(13) Xia, Y.; Gilroy, K. D.; Peng, H.-C.; Xia, X. Seed-Mediated Growth of Colloidal Metal Nanocrystals. *Angewandte Chemie International Edition* **2017**, *56* (1), 60-95. DOI: doi:10.1002/anie.201604731.
(14) Rossi, L. M.; Fiorio, J. L.; Garcia, M. A. S.; Ferraz, C. P. The role and fate of capping ligands in colloidally prepared metal nanoparticle catalysts. *Dalton Transactions* **2018**, *47* (17), 5889-5915, 10.1039/C7DT04728B. DOI: 10.1039/C7DT04728B.
(15) Lopez, N.; Janssens, T. V. W.; Clausen, B. S.; Xu, Y.; Mavrikakis, M.; Bligaard, T.; Nørskov, J. K. On the origin of the catalytic activity of gold nanoparticles for low-temperature CO oxidation. *Journal of Catalysis* **2004**, *223* (1), 232-235. DOI: https://doi.org/10.1016/j.jcat.2004.01.001.

(16) Burda, C.; Chen, X. B.; Narayanan, R.; El-Sayed, M. A. Chemistry and properties of nanocrystals of different shapes. *Chemical Reviews* **2005**, *105* (4), 1025-1102. DOI: 10.1021/cr030063a.
(17) Jain, P. K.; Lee, K. S.; El-Sayed, I. H.; El-Sayed, M. A. Calculated Absorption and Scattering Properties of Gold Nanoparticles of Different Size, Shape, and Composition: Applications in Biological Imaging and Biomedicine. *The Journal of Physical Chemistry B* **2006**, *110* (14), 7238-7248. DOI: 10.1021/jp057170o.
(18) Link, S.; El-Sayed, M. A. Spectral Properties and Relaxation Dynamics of Surface Plasmon Electronic Oscillations in Gold and Silver Nanodots and Nanorods. *The Journal of Physical Chemistry B* **1999**, *103* (40), 8410-8426. DOI: 10.1021/jp9917648.
(19) Creighton, J. A.; Eadon, D. G. Ultraviolet–visible absorption spectra of the colloidal metallic elements. *Journal of the Chemical Society, Faraday Transactions* **1991**, *87* (24), 3881-3891, 10.1039/FT9918703881. DOI: 10.1039/FT9918703881.
(20) Linic, S.; Chavez, S.; Elias, R. Flow and extraction of energy and charge carriers in hybrid plasmonic nanostructures. *Nature Materials* **2021**, *20* (7), 916-924. DOI: 10.1038/s41563-020-00858-4.
(21) Brongersma, M. L.; Halas, N. J.; Nordlander, P. Plasmon-induced hot carrier science and technology. *Nature Nanotechnology* **2015**, *10*, 25, Review Article. DOI: 10.1038/nnano.2014.311.
(22) Brown, A. M.; Sundararaman, R.; Narang, P.; Goddard, W. A.; Atwater, H. A. Nonradiative Plasmon Decay and Hot Carrier Dynamics: Effects of Phonons, Surfaces, and Geometry. *ACS Nano* **2016**, *10* (1), 957-966. DOI: 10.1021/acsnano.5b06199.
(23) Mao, Z.; Vang, H.; Garcia, A.; Tohti, A.; Stokes, B. J.; Nguyen, S. C. Carrier Diffusion—The Main Contribution to Size-Dependent Photocatalytic Activity of Colloidal Gold Nanoparticles. *ACS Catal.* **2019**, *9* (5), 4211-4217. DOI: 10.1021/acscatal.9b00390.
(24) Redmond, P. L.; Brus, L. E. "Hot Electron" Photo-Charging and Electrochemical Discharge Kinetics of Silver Nanocrystals. *The Journal of Physical Chemistry C* **2007**, *111* (40), 14849-14854. DOI: 10.1021/jp0741859.
(25) Henglein, A. The Reactivity of Silver Atoms in Aqueous Solutions (A γ-Radiolysis Study). *Berichte der Bunsengesellschaft für physikalische Chemie* **1977**, *81* (6), 556-561. DOI: https://doi.org/10.1002/bbpc.19770810604.
(26) Scanlon, M. D.; Peljo, P.; Méndez, M. A.; Smirnov, E.; Girault, H. H. Charging and discharging at the nanoscale: Fermi level equilibration of metallic nanoparticles. *Chem. Sci.* **2015**, *6* (5), 2705-2720, 10.1039/C5SC00461F. DOI: 10.1039/C5SC00461F.
(27) Mulvaney, P.; Pérez-Juste, J.; Giersig, M.; Liz-Marzán, L. M.; Pecharromán, C. Drastic Surface Plasmon Mode Shifts in Gold Nanorods Due to Electron Charging. *Plasmonics* **2006**, *1* (1), 61-66. DOI: 10.1007/s11468-005-9005-0.
(28) Kolb, D. M.; Engelmann, G. E.; Ziegler, J. C. On the Unusual Electrochemical Stability of Nanofabricated Copper Clusters. *Angewandte Chemie International Edition* **2000**, *39* (6), 1123-1125. DOI: https://doi.org/10.1002/(SICI)1521-3773(20000317)39:6<1123::AID-ANIE1123>3.0.CO;2-#.
(29) Del Pópolo, M. G.; Leiva, E. P. M.; Mariscal, M.; Schmickler, W. The basis for the formation of stable metal clusters on an electrode surface. *Nanotechnology* **2003**, *14* (9), 1009. DOI: 10.1088/0957-4484/14/9/314.

(30) Ward Jones, S. E.; Campbell, F. W.; Baron, R.; Xiao, L.; Compton, R. G. Particle Size and Surface Coverage Effects in the Stripping Voltammetry of Silver Nanoparticles: Theory and Experiment. *The Journal of Physical Chemistry C* **2008**, *112* (46), 17820-17827. DOI: 10.1021/jp807093q.
(31) Ivanova, O. S.; Zamborini, F. P. Electrochemical Size Discrimination of Gold Nanoparticles Attached to Glass/Indium−Tin-Oxide Electrodes by Oxidation in Bromide-Containing Electrolyte. *Analytical Chemistry* **2010**, *82* (13), 5844-5850. DOI: 10.1021/ac101021q.
(32) Ivanova, O. S.; Zamborini, F. P. Size-Dependent Electrochemical Oxidation of Silver Nanoparticles. *Journal of the American Chemical Society* **2010**, *132* (1), 70-72. DOI: 10.1021/ja908780g.
(33) Kumar, A.; Buttry, D. A. Size-Dependent Anodic Dissolution of Water-Soluble Palladium Nanoparticles. *The Journal of Physical Chemistry C* **2013**, *117* (50), 26783-26789. DOI: 10.1021/jp408394h.
(34) Tang, L.; Han, B.; Persson, K.; Friesen, C.; He, T.; Sieradzki, K.; Ceder, G. Electrochemical Stability of Nanometer-Scale Pt Particles in Acidic Environments. *Journal of the American Chemical Society* **2010**, *132* (2), 596-600. DOI: 10.1021/ja9071496.
(35) Brainina, K. Z.; Galperin, L. G.; Vikulova, E. V. Electrochemistry of metal nanoparticles: the effect of substrate. *Journal of Solid State Electrochemistry* **2012**, *16* (7), 2357-2363. DOI: 10.1007/s10008-012-1721-8.
(36) Masitas, R. A.; Khachian, I. V.; Bill, B. L.; Zamborini, F. P. Effect of Surface Charge and Electrode Material on the Size-Dependent Oxidation of Surface-Attached Metal Nanoparticles. *Langmuir* **2014**, *30* (43), 13075-13084. DOI: 10.1021/la5029614.

Ch 2 - The Nernst equation at the nanoscale: probing the size and surfactant effects on the AuNP reduction potentials

Introduction

Determining the reduction or oxidation potentials of noble metal NPs is important for understanding their electrochemical properties, synthesizing their nanocrystal structures from redox reactions, and developing their catalytic applications. In many cases, measuring the redox potentials when the NPs are in colloidal form is critical. Powerful electrochemical techniques like anodic striping voltammetry have made it possible to investigate the NP oxidation potentials in relation to size,[1, 2] elemental compositions,[3] surface charge,[4] and dispersity.[5, 6] While voltammetry techniques have their own advantages, they require the loading of the NPs onto the electrodes. The NP-electrode interactions alter the NP redox potentials in many different ways, depending on the nature of the interactions. The direct contact between the NPs and electrodes causes charge exchange to keep the same Fermi levels of the two materials.[4, 6, 7] The shift of the NP redox potentials strongly depends on the work function difference between the two materials. When there are linkers between the NPs and electrodes, the surface charge and chemical materials of the electrodes also shift the NP redox potentials.[7] Here, we develop a contactless method for measuring the standard reduction potentials of colloidal NPs that avoid the influence of the electrodes. This approach allows us to accurately quantify their standard reduction potentials concerning their size.

At the nanoscale, the NP reduction potentials are dependent on their size. For example, early work by Henglein demonstrated an increasing electrochemical reactivity in Ag clusters, estimating a large drop in the reduction potential from +0.799 V (bulk value) down to -1.7 V (single atom).[8] Plieth theorized these negative shifts were caused by the changes in free energy associated with the change in surface area from the bulk to NPs.[9] Early measurements of the dissolution of metallic NPs using scanning tunneling microscopy measured a shift in potential from the bulk that contradicted Plieth's equation and was attributed to quantum effects. [10] Other reports provided further evidence that mechanical alloying, not quantum effects, was the reason for the contradictory observations.[11-13] Zamborini and co-workers later presented a systematic method of measuring the change in oxidation potential of AgNPs using linear sweep voltammetry that definitively revealed a size-dependent trend.[1]

Similar size-dependent trends were found on AuNPs, PdNPs, and PtNP, albeit with some deviations.[2, 14, 15] These small deviations were attributed to various factors, including a change in NP surface tension, exposed crystallographic faces, and surface passivation.[1, 2, 15] However, surface interactions between the electrode and the NP can also contribute a shift in potentials. When NPs interact with the substrate, their surface Gibbs free energy will change due proportionally to the difference in their work functions materials.[7] These interfacial interactions can be mitigated by electrostatically anchoring the NPs onto the electrode using molecular linkers. However, supporting the NPs using charged linkers also influence the reduction potentials due to electrostatic effects on the NP-electrode interface.[4] It is possible these substrate interactions could obscure other effects such as those introduced by the capping ligands and surrounding medium.

The capping ligands used to stabilize the NPs also influence their reduction potentials. Popular stabilizers like CTAB have been employed for synthesizing a variety

of NPs of different shapes like rods.[16] However, these surfactants have been speculated to induce a strong shift in the NP potential. The high binding constant the micelles and the gold complex, whether a product of oxidation or synthesis precursor, is thought to be the reason for the shift in potential.[17, 18] The shift in potential is predicted to be as much as 600 mV lower than the bulk and would explain why popular etchants such as Fe^{3+} can etch noble metals like AuNPs, which are otherwise unfavorable according to their standard reduction potentials.[18] To the best of our knowledge, the shift in potential induced by quaternary ammonium surfactants has not been measured.

Through the Galvanic equilibrium approach, we quantified the standard reduction potentials and examined the size and surfactant effects. Our results demonstrated a size dependence on the standard reduction potentials of CTAB/C-stabilized AuNPs and followed an inverse radius trend as previously theorized. Furthermore, we observed a large shift in the standard reduction potential of AuNPs owing to the strong interactions between the cationic surfactant and $AuBr_2^-$ complexes. The presence of the micelles also plays a kinetic role in the etching and regrowth process. These findings demonstrate Galvanic equilibration as a power technique for probing the electrochemical properties of NPs in response to changes in size and local environment. With some modification, this approach can potentially probe NPs of different sizes, shapes, and compositions in colloidal states.

Results and Discussion

The Nernst equation at the nanoscale

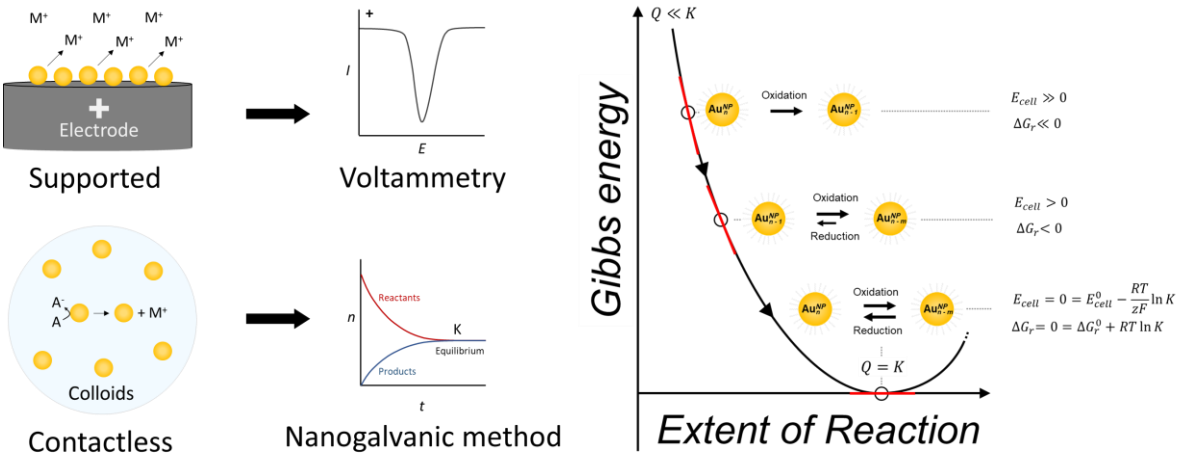

Figure 1. (a) In a typical ASV measurement, the electrical current given by the dissolution or "stripping" of metallic NPs supported on the working electrode is measured by applying a potential. The potential of maximum current corresponds to the peak oxidation potential of the NP ensemble. (b) In a nanogalvanic equilibration reaction, colloidal NPs are allowed to react with a redox species until an equilibrium is established. Once at equilibrium, the reaction equilibrium constant can be determined. (c) The forward reaction is spontaneous in the direction of decreasing Gibbs energy or cell potential. When the cell potential is equal to zero, the reaction is considered equilibrated. With the equilibrium constant, the standard reduction potential can is calculated using the Nernst equation.

The NP redox potentials can be evaluated through voltammetry or by equilibration. In voltammetry, NPs are supported on the electrode surfaces and are stripped (oxidized) with an applied potential, generating a current peak centered at the oxidation potential (Figure 1a). As mentioned in the introduction section, the electrodes can alter the actual oxidation potentials of the NPs. To avoid the influence from the electrodes, the reduction potential measurement must be conducted for the colloidal from of the NPs (Figure 1b). This contactless method can be achieved by establishing a redox reaction between the colloidal NPs and another redox couple. For convenient chemical analysis, $Fe^{3+/2+}$ was used, and the reaction at equilibrium is written as follows.

$$Fe^{3+} + e^- \rightarrow Fe^{2+} \qquad E^0 = +\,0.771\ \text{V} \qquad (1)$$

$$Au^+ + e^- \rightarrow Au^0(s) \qquad E^0 = +\,1.83\ \text{V} \qquad (2)$$

$$AuBr_2^- + e^- \rightarrow Au^0(s) + 2Br^- \qquad E^0 = +\,0.96\ \text{V} \qquad (3)$$

From the given reaction conditions, the chemical equations are summarized as follows:

$$AuNP_n(s) + Fe^{3+} \rightleftharpoons AuNP_{n-1}(s) + Fe^{2+} + Au^{+} \quad (4)$$

$$Au^{+} + 2Br^{-} \rightarrow AuBr_2^{-} \quad (5)$$

$$AuBr_2^{-} + CTA^{+} \rightarrow AuBr_2CTA(s) \quad (6)$$

Finally, the net chemical equation is summarized as:

$$AuNP_n(s) + Fe^{3+} + 2Br^{-} + CTA^{+} \rightleftharpoons AuNP_{n-1}(s) + Fe^{2+} + AuBr_2CTA(s) \quad (7)$$

We propose that the Nernst equation can be used for the above reaction to measure the NP redox potentials, here called the Galvanic equilibration method. However, there are some conditions for applying this method because the Nernst equation has been used only for bulk electrodes. Under a typical electrochemical-cell setup, the two half-cell reactions are separated, and the two corresponding electrodes are electrically connected. When the half-cell reactions establish, the Nernst equation can be used to calculate the electrode potentials for these macroscopic electrodes. To use this equation for colloidal NPs, the two haft-cell reactions must happen on individual NPs. Although there is no conversion of chemical to electrical energy in this system, and there is not an actual cell potential, reaction (1), constituting the "half-cell" reactions (2) and (3), does happen and eventually must reach an equilibrium. At the equilibrium point, the reaction Gibbs free energy must be zero and the reduction potentials involved in the two half-cell reactions must be equal. Another way to interpret this result is the individual NPs can act like the two electrodes and an imaginary E_{cell} must be zero at equilibrium (Figure 1c). Hence, the Nernst equation can be used at the equilibrium point:

$$[E^0_{AuBr_2CTA/Au}]^{NP_n} = E^0_{Fe^{3+}/Fe^{2+}} - \frac{RT}{zF} ln \frac{[Fe^{2+}]}{[Fe^{3+}][Br^{-}]^2[CTA^{+}]} \quad (8)$$

Here, $[E^0_{AuBr_2CTA/Au}]^{NP_n}$ is the standard reduction potential of the AuNP, where *n* signifies the number of gold atoms per nanoparticle, $E^0_{Fe^{3+}/Fe^{2+}}$ is the standard reduction potential of the $Fe^{3+/2+}$ redox couple, R is the ideal gas constant, T is the temperature in Kelvin, z is the number of electrons transferred, and F is Faraday's constant. From these constants, the $[E^0_{AuBr_2CTA/Au}]^{NP_n}$ can then be calculated using the reaction equilibrium concentrations.

Redox reaction equilibria of the AuNPs and Fe^{3+}

We prepared a series of reaction solutions consisting of Fe^{3+} and spherical AuNPs of various diameters stabilized by CTAB/C to establish the reaction equilibria. Figure 2 is a scheme that summarizes the redox reaction between the AuNPs and the $Fe^{3+/2+}$ redox couple. Unless otherwise stated, the CTA^+ concentration was maintained above the CMC, the total colloidal Au^0 was maintained between 0.20 ~ 0.26 mM, and the Fe^{3+} concentration was kept at 0.27 mM Fe^{3+}. Since Fe^{3+} is prone to hydrolysis in basic conditions, the pH of all the solutions was maintained at approximately pH 2 using HCl.

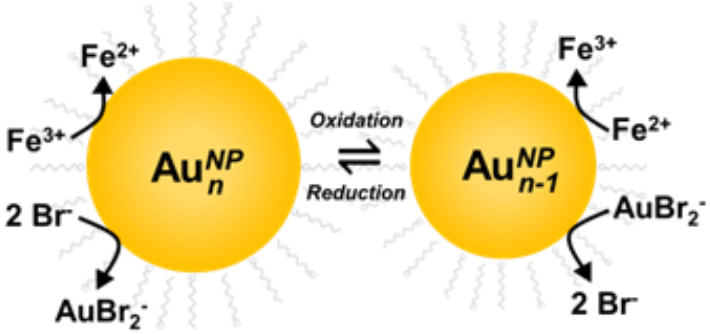

Figure 2. Representation of the oxidation and reduction equilibrium of the $AuBr_2^-$ /AuNPs and the $Fe^{3+/2+}$ couples. For clarity, CTA^+ was shaded light grey and its halide counter ions were omitted for simplicity.

Furthermore, all solutions were purged with dinitrogen to remove atmospheric oxygen and prevent Fe^{2+} from reverting back to Fe^{3+}. At the start of the reaction, Fe^{3+} oxidizes the AuNPs resulting in a gradual reduction in volume. This reduction in volume is evident as a decay of LSPR in the UV-Vis spectra (Figure 3a). Although Fe^{3+} has some absorbance in the visible, its electronic transitions begin at 440 nm, thus avoiding optical overlap with the LSPR. Plotting the absorbance at the LSPR maximum over time yields kinetic traces that slowly decay until no further net change is observed (Figure 3b). At this state, the rate of regrowth becomes approximately equal to the rate of etching, thus indicating an equilibrium.

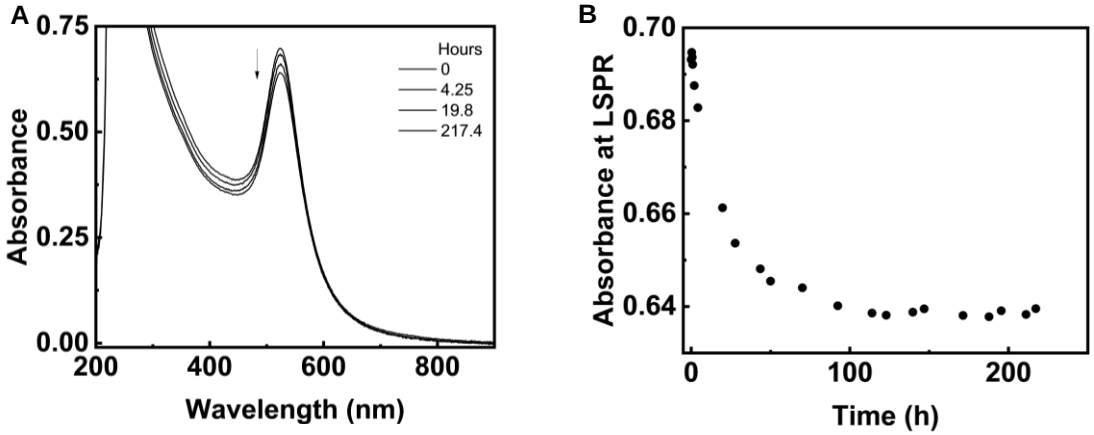

Figure 3. (A) Representative UV-Vis absorbance spectrum of the redox reaction between Fe^{3+} and 11.3 nm AuNPs and (B) respective kinetic traces plotted from the same reaction as the extinction at the LSPR over time.

The time to reach an equilibrium varied with particle size, but in general, the reaction rate was kinetically slower for the large AuNPs. These rate differences could be due to two reasons. One, the initial rate was higher for the smaller diameters due to their total surface area from the greater number of AuNPs in the solutions. A greater number of AuNPs are necessary to maintain the total colloidal Au^0 between ~0.20-0.25 mM for the smaller diameters. Two, smaller particles possess greater curvature. CTAB is known to stabilize the AuNPs through a positive electrostatic surface charge, thus a greater curvature decreases the charge density and allows the Fe^{3+} to diffuse toward the surface more freely than large particles with less curvature. Similar observations have been reported on Au nanorods to explain the preferential growth or etching at the tips.

AuNP standard reduction potentials

After reaching equilibrium, the concentration of the Fe^{2+} was evaluated through chemical assays and UV-Vis. To measure the total Fe^{2+} in the reaction solutions, the well-known 1,10-phenanthroline (PT) chemical assay was employed. In this test, PT forms a $Fe(PT)_3^{2+}$ complex with a molar absorptivity coefficient of 1.13×10^4 M^{-1} cm^{-1} at 511 nm whose concentration can be accurately determined using UV-Vis spectroscopy. The molar absorptivity of $Fe(PT)_3^{2+}$ was determined using a standard curve consisting of Fe^{2+} stock solutions with known concentrations (see Appendix 1). Using this method, we found that the total Fe^{2+} increased as the AuNP diameter decreased. For example, in the 4.4 nm AuNPs the average Fe^{2+} was 95.0 μM but was 16.5 μM for the larger 74 nm AuNPs (Figure 4). This difference in Fe^{2+} suggests that small AuNPs are more prone to oxidation by Fe^{3+} than larger AuNPs.

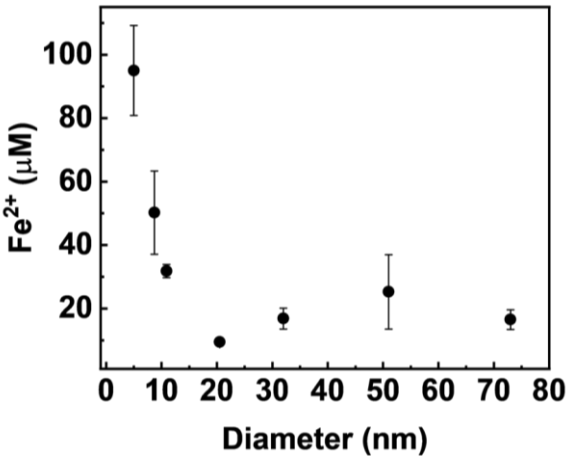

Figure 4. The average equilibrium Fe^{2+} measured in each reaction with 4 nm, 8.6 nm, 11.3 nm, 21.2 nm, 32.8 nm, 52 nm, and 74 nm AuNPs. Error bars correspond to the standard deviation.

From the measured Fe^{2+}, the concentration of the remaining species was stoichiometrically calculated for each reaction. First, the concentration of Fe^{3+} was stoichiometrically determined from the difference of the initial Fe^{3+} and the measured Fe^{2+}. Similarly, the remaining Br^- was calculated from the initial concentration of CTAB (1.1 mM) and total $AuBr_2CTA$ produced, which is also stoichiometrically equal of Fe^{2+} (see Equation 7).

Alternatively, the total colloidal Au can be estimated based on the AuNP extinction. For plasmonic NPs, the extinction at the LSPR is proportional to volume, thus can be used to estimate the total colloidal Au^0 oxidized from etching (see Appendix 1 for calculations). Interestingly, this approach yields $AuBr_2^-$ values not stoichiometrically equal to Fe^{2+} (reaction 7). This discrepancy may stem from inaccuracies associated with using the LSPR for quantifying Au^0. Small variations in particle shape, dielectric environment, surface chemistry and particle proximity are among many factors that can affect the position and height of the LSPR peak.[19] Therefore, spectra between AuNPs can only be compared when they are physically and chemically similar. Another approach is to use the extinction within the optical interband region of Au since it is less sensitive to such external factors, however this yielded values lower than Fe^{2+}. Due to such uncertainties, we believe using the Fe^{2+} values obtained from chemical assays to stoichiometrically estimate the total $AuBr_2^-$ in the reaction solutions would be more appropriate.

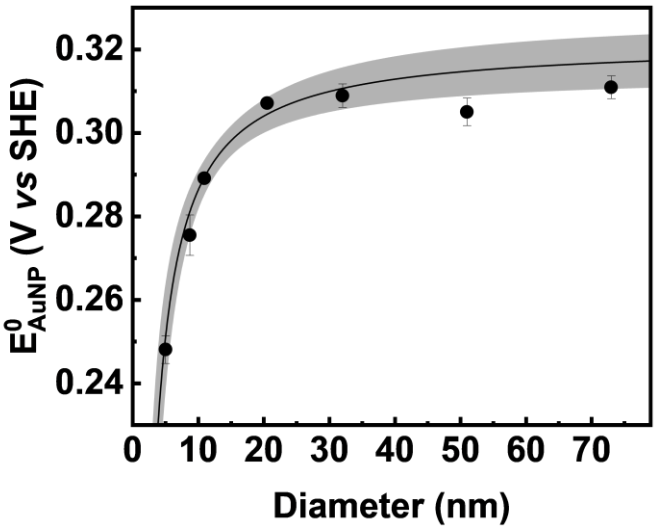

Figure 5. The $[E^0_{AuBr_2CTA/Au}]^{NP_n}$ of 4.4 nm – 74 nm AuNPs calculated using Nernst. The standard error is shown as bars and the 95% confidence band is shaded in gray.

To calculate the standard reduction potentials using the Nernst equation, the equilibrium concentrations of the products and reactants were substituted into Equation 8. For the equilibrium concentration of CTA^+, we treated the monomeric concentration as the real concentration in the reaction solution. Incorporating the total concentration (including micelles) rather than the monomeric concentrations leads to $[E^0_{AuBr_2CTA/Au}]^{NP_n}$ values above the theoretical predictions. To validate our approach, we ran a series of controls with different CTA^+ concentrations (see SI). From the controls, the equilibrium Fe^{2+} in the reactions did not significantly change across concentrations well above the CMC. This suggests that the reactions are thermodynamically independent of micellar CTA^+, thus only the monomeric CTA^+ was used in the calculations. These calculations lead to $[E^0_{AuBr_2CTA/Au}]^{NP_n}$ values that ranged from 0.248 V to 0.311 V for diameters between 4.4 nm and 74 nm, respectively. Plotting $[E^0_{AuBr_2CTA/Au}]^{NP_n}$ against the diameter yields a trend resembling 1/r, with potentials increasingly becoming negative as the AuNP size decreases. However, little change in the $[E^0_{AuBr_2CTA/Au}]^{NP_n}$ is observed above ~20 nm, indicating bulk-like behavior in AuNPs above those diameters.

To determine the standard bulk reduction potential of the $AuBr_2CTA$ species, the $[E^0_{AuBr_2CTA/Au}]^{NP_n}$ values were linearly fitted as a function of 1/r (see SI). Such fit yielded an intercept representing the bulk reduction potential of 0.319 V. To our best knowledge, this standard reduction potential for the $AuBr_2CTA$ species has yet to be experimentally reported, but previous estimates by Liz-Marzán has predicted a cathodic shift by as much as 0.6 V for the Au(I) species in the presence of CTAB, yielding a potential of 0.4 V.[16] In our case, the cathodic shift is approximately 0.641 V and thus in agreement with prior predictions. This potential shift is due to a precipitation effect by the $AuBr_2CTA$ ion pair,

which tilts the reaction equilibrium towards the product's side. For example, in complexes such as $AuCl_4^-$, solubility product constants are as low as 10^{-12} M^2, rendering them insoluble. This solubility issue can be avoided by keeping the surfactant concentration high to allow the micelles to solubilize the $AuBr_2CTA$. As such, the micelles play an important kinetic role and without them, the reaction becomes kinetically sluggish.

Kinetic and thermodynamic role of micellar CTA^+

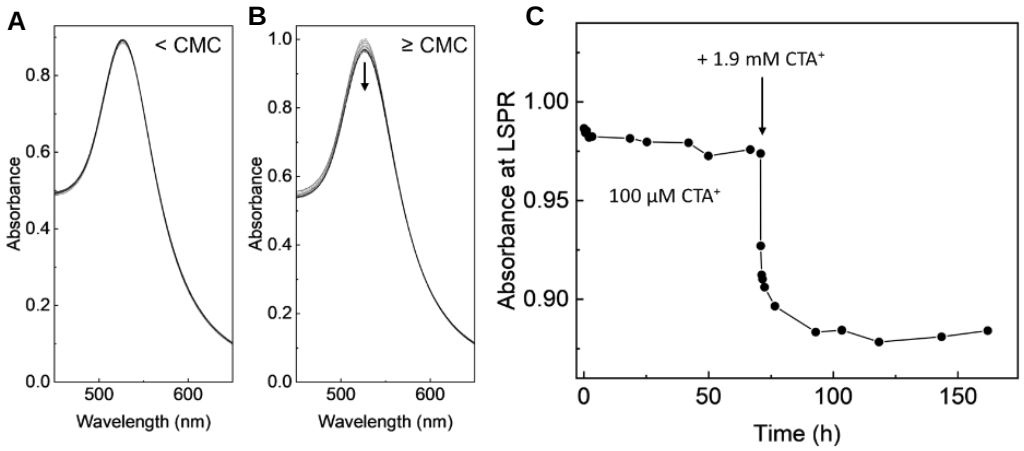

Figure 6. Time-lapsed UV-Vis spectra of the redox reaction of the 10 nm AuNPs and $FeCl_3$ when the CTA^+ concentration is at (A) 0.50 mM or (B) 0.96 mM. (C) Kinetics trace plot of the same reaction except the concentration of CTA^+ is 0.1 mM in the first 70 h, but then is increased to 2 mM by injecting additional CTA^+.

To understand the role of CTA^+ on the oxidative etching of AuNP, we performed a series of redox reactions with the AuNPs and $FeCl_3$ in different surfactant concentrations. Interestingly, we found that the oxidative etching of the AuNPs by Fe^{3+} depended on the total concentration of the CTA^+. When the concentration of CTA^+ was adjusted to 0.50 mM CTA^+, the extinction at the LSPR remained constant and no signs of $AuBr_2CTA$ precipitation were observed over five days (Figure 6a). Thus, such observations strongly suggest that little to no etching had occurred. However, when the concentration was raised to 0.96 mM, approximately the CMC of CTAB, etching was observed (Figure 6b). This observation strongly suggests that the micelles play a critical kinetic role in the reaction. To further support this hypothesis, another reaction solution was prepared with CTA^+ concentration far below the CMC (0.10 mM) and allowed to progress over 70 hours. Again, AuNP etching was not evident. Then, an additional 1.9 mM CTA^+ was added to the same reaction mixture so the concentration was well above the CMC. Immediately after injection, the AuNPs were observed to undergo etching (Figure 6c). Such observation further confirms that the micelles kinetically accelerate the reactions.

Based on our observations, we propose that the CTA^+ micelles shuttle the $AuBr_2^-$ between the AuNP and the solution during the reaction with Fe^{3+}. Shuttling of the $AuBr_2^-$ is possible due to the strong electrostatic attraction with the CTA^+ on the micelle. This strong attraction yields solubility product constants as high as 10^{-12} M^2 for complexes such as $AuCl_4^-$ with low solubility.[17] This low solubility issue is typically avoided under high surfactant concentrations, where the micelles solubilize the gold complex-surfactant ion pairs. This description would explain why the redox reaction between AuNPs and Fe^{3+} was very slow below the CMC. However, this left us wondering if they also have any thermodynamic effect on the $[E^0_{AuBr_2CTA/Au}]^{NP_n}$.

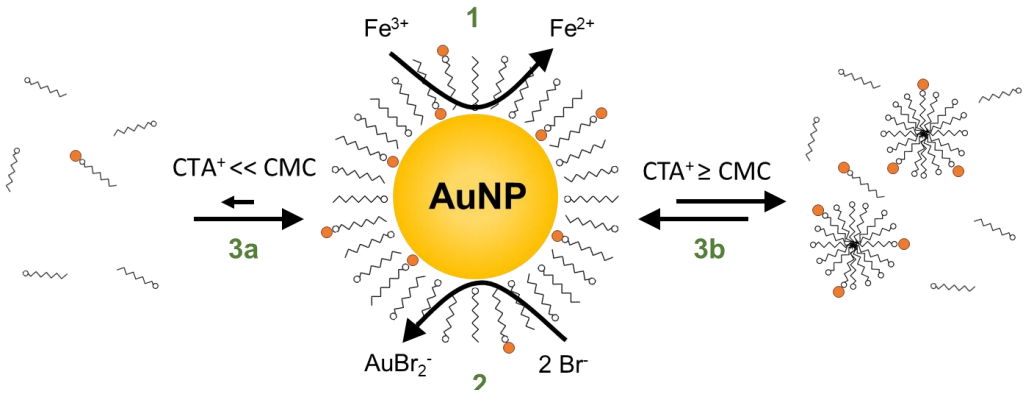

Figure 7. Scheme of the reaction steps in during the equilibration of the nanogalvanic reaction. First, Fe^{3+} is reduced to Fe^{2+} by the AuNPs. Oxidation of the AuNPs generates the $AuBr_2^-$ complexes and form ion pairs with CTA^+. The rate of this reaction is determined by the presences of CTA^+ micelles which act shuttle the $(CTA)AuBr_2$ ion pairs into the solution as the AuNPs are oxidized by Fe^{3+}. Without the micelles, the reaction is kinetically sluggish.

Conclusion

In conclusion, the standard redox potentials NPs can be evaluated using either voltammetry or equilibration. Galvanic equilibration is a method that couples the NPs with a redox species and allows the reaction to reach an equilibrium, from which the standard Gibbs free energy of the reaction or the standard reduction potential of the reaction can be determined. The equilibration method was used to evaluate the standard reduction potentials of AuNPs using $Fe^{3+/2+}$ as the redox couple. The redox reactions were allowed to reach equilibrium across multiple particle sizes through careful control of the reaction components and conditions. The AuNP absorbance at LSPR was used to monitor the equilibration progress of the reactions using UV-Vis spectroscopy. The reaction rate varied with particle size, with smaller particles having higher initial rates due to a combination of factors, including greater number of particles, large curvature, and large surface area. After reaching equilibrium, the concentration of the products and reactants were evaluated through chemical assay and UV-Vis spectroscopy. Then, using the Nernst equation, the reduction potential for each size of NP was determined.

Here, we found the reduction potentials to follow the theoretical trends as predicted by Plieth. The reduction potentials followed an inverse radius trend, increasing from 0.248 V to 0.311 V for diameters between 4.4 nm and 74 nm, respectively. This trend can be attributed to increased surface energy as the NP radius decreases. In smaller diameters, a larger number of unsaturated gold atoms with greater energy is exposed, thus the overall surface energy increases and is observed as a negative shift in the reduction potential.

Furthermore, the CTA^+ surfactant was observed to play a critical thermodynamic and kinetic role. The CTA^+ surfactant electrostatically interacts with the $AuBr_2^-$ species to the $(CTA)AuBr_2$ ion pair with a low solubility product constant. This low solubility product constant drastically shifts the reaction equilibrium to favor the products and, consequently, lowers the reduction potential. Additionally, the presence of micelles kinetically enhances the reaction rate by facilitating the transport of the gold complex products into the solution. In the absence of micelles, the reactions were kinetically sluggish.

In summary, galvanic equilibration of the NPs was demonstrated to be an effective method for measuring the standard reduction potentials of colloidal AuNPs as a function of size. Furthermore, this approach showed how particle size and local environment changes affect the reduction potential. With this approach, we anticipate that other physical and chemical that are predicted to contribute to the reduction potential (e.g., crystallographic shape) can be explored.

Ch. 2 References

(1) Ivanova, O. S.; Zamborini, F. P. Size-Dependent Electrochemical Oxidation of Silver Nanoparticles. *Journal of the American Chemical Society* **2010**, *132* (1), 70-72. DOI: 10.1021/ja908780g.
(2) Ivanova, O. S.; Zamborini, F. P. Electrochemical Size Discrimination of Gold Nanoparticles Attached to Glass/Indium−Tin-Oxide Electrodes by Oxidation in Bromide-Containing Electrolyte. *Analytical Chemistry* **2010**, *82* (13), 5844-5850. DOI: 10.1021/ac101021q.
(3) Pattadar, D. K.; Zamborini, F. P. Halide-Dependent Dealloying of Cux/Auy Core/Shell Nanoparticles for Composition Analysis by Anodic Stripping Voltammetry. *The Journal of Physical Chemistry C* **2019**, *123* (14), 9496-9505. DOI: 10.1021/acs.jpcc.8b12174.
(4) Masitas, R. A.; Khachian, I. V.; Bill, B. L.; Zamborini, F. P. Effect of Surface Charge and Electrode Material on the Size-Dependent Oxidation of Surface-Attached Metal Nanoparticles. *Langmuir* **2014**, *30* (43), 13075-13084. DOI: 10.1021/la5029614.
(5) Pattadar, D. K.; Zamborini, F. P. Effect of Size, Coverage, and Dispersity on the Potential-Controlled Ostwald Ripening of Metal Nanoparticles. *Langmuir* **2019**, *35* (50), 16416-16426. DOI: 10.1021/acs.langmuir.9b02421.
(6) Pattadar, D. K.; Sharma, J. N.; Mainali, B. P.; Zamborini, F. P. Anodic stripping electrochemical analysis of metal nanoparticles. *Current Opinion in Electrochemistry* **2019**, *13*, 147-156. DOI: https://doi.org/10.1016/j.coelec.2018.12.006.
(7) Brainina, K. Z.; Galperin, L. G.; Vikulova, E. V. Electrochemistry of metal nanoparticles: the effect of substrate. *Journal of Solid State Electrochemistry* **2012**, *16* (7), 2357-2363. DOI: 10.1007/s10008-012-1721-8.
(8) Henglein, A. The Reactivity of Silver Atoms in Aqueous Solutions (A γ-Radiolysis Study). *Berichte der Bunsengesellschaft für physikalische Chemie* **1977**, *81* (6), 556-561. DOI: https://doi.org/10.1002/bbpc.19770810604.
(9) Plieth, W. J. Electrochemical properties of small clusters of metal atoms and their role in the surface enhanced Raman scattering. *The Journal of Physical Chemistry* **1982**, *86* (16), 3166-3170. DOI: 10.1021/j100213a020.
(10) Kolb, D. M.; Engelmann, G. E.; Ziegler, J. C. On the Unusual Electrochemical Stability of Nanofabricated Copper Clusters. *Angewandte Chemie International Edition* **2000**, *39* (6), 1123-1125. DOI: https://doi.org/10.1002/(SICI)1521-3773(20000317)39:6<1123::AID-ANIE1123>3.0.CO;2-#.
(11) Nielinger, M.; Baltruschat, H. Local Formation of an Alloy by Atomic Contact between the STM Tip and the Substrate Surface. *ChemPhysChem* **2003**, *4* (9), 1022-1024. DOI: https://doi.org/10.1002/cphc.200300820.
(12) Maupai, S.; Dakkouri, A. S.; Stratmann, M.; Schmuki, P. Tip-Induced Nanostructuring of Au3Cu (001) with an Electrochemical Scanning Tunneling Microscope. *J Electrochem Soc* **2003**, *150* (3), C111. DOI: 10.1149/1.1541007.
(13) Popolo, M. D.; Leiva, E.; Kleine, H.; Meier, J.; Stimming, U.; Mariscal, M.; Schmickler, W. Generation of palladium clusters on Au(111) electrodes: Experiments

and simulations. *Applied Physics Letters* **2002**, *81* (14), 2635-2637. DOI: 10.1063/1.1511285.
(14) Kumar, A.; Buttry, D. A. Size-Dependent Anodic Dissolution of Water-Soluble Palladium Nanoparticles. *The Journal of Physical Chemistry C* **2013**, *117* (50), 26783-26789. DOI: 10.1021/jp408394h.
(15) Tang, L.; Han, B.; Persson, K.; Friesen, C.; He, T.; Sieradzki, K.; Ceder, G. Electrochemical Stability of Nanometer-Scale Pt Particles in Acidic Environments. *Journal of the American Chemical Society* **2010**, *132* (2), 596-600. DOI: 10.1021/ja9071496.
(16) Pérez-Juste, J.; Liz-Marzán, L. M.; Carnie, S.; Chan, D. Y. C.; Mulvaney, P. Electric-Field-Directed Growth of Gold Nanorods in Aqueous Surfactant Solutions. *Advanced Functional Materials* **2004**, *14* (6), 571-579. DOI: https://doi.org/10.1002/adfm.200305068.
(17) Ishizuka, H.; Tano, T.; Torigoe, K.; Esumi, K.; Meguro, K. Preparation of monodispersed colloidal gold by reduction of AuCl−4—cationic surfactant complexes. *Colloids and Surfaces* **1992**, *63* (3), 337-340. DOI: https://doi.org/10.1016/0166-6622(92)80256-2.
(18) Rodríguez-Fernández, J.; Pérez-Juste, J.; Mulvaney, P.; Liz-Marzán, L. M. Spatially-Directed Oxidation of Gold Nanoparticles by Au(III)−CTAB Complexes. *The Journal of Physical Chemistry B* **2005**, *109* (30), 14257-14261. DOI: 10.1021/jp052516g.
(19) Hendel, T.; Wuithschick, M.; Kettemann, F.; Birnbaum, A.; Rademann, K.; Polte, J. In Situ Determination of Colloidal Gold Concentrations with UV–Vis Spectroscopy: Limitations and Perspectives. *Analytical Chemistry* **2014**, *86* (22), 11115-11124. DOI: 10.1021/ac502053s.

Ch. 3 - Tuning Redox Potential of Gold Nanoparticle Photocatalysts by Light

Introduction

Using photocatalysts to accelerate chemical reactions is an important option to explore for new catalytic activities, chemical syntheses with less heat waste, and utilizing photons from either the sun or artificial lights. Recently, metallic nanoparticles (NP) have gained growing interest for applications in photocatalysis.[1-15] In general, transition metal NPs can absorb photons in the ultraviolet to visible region due to the intrinsic *d*-to-*sp* electronic interband transitions. Noble metal NPs (such as those of Au, Ag, and Cu) have additional strong absorption bands in the visible region due to the localized surface plasmon resonance (LSPR). As a result of these optical excitations, hot electrons and holes are generated and migrate to the surface of the NPs through scattering to catalyze chemical transformations of adsorbed reactants.[16, 17] Other catalytic mechanisms, such as those through field enhancement[4] or heating,[18] are also possible depending on the experimental conditions. A special advantage of metallic NP photocatalysts is that their activities and selectivities could be tuned by changing the excitation wavelength.[8, 19-22] One main reason for this is that the energy distribution of the photogenerated hot carriers is wavelength dependent. This unique feature comes from the lack of a band gap in metal. For other photocatalysts, such as semiconductor NPs,[23, 24] transition metal chromophores,[25] or organic photoredox compounds,[26] their catalytic activities are strongly restricted by the energy gaps between their valence bands and conduction bands or between ground states and excited states. Thus, tuning their catalytic activities requires the redesign or modification of catalyst structures or material contents. The unique wavelength dependence of activities and selectivities gives metallic NPs a great potential in the fine tuning of catalysis for each suitable chemical reaction.

In this work, our approach for tuning metallic NPs' photocatalytic activity is based on the selective quenching of hot holes (or hot electrons) which leads to the accumulation of ground state electrons (or holes) and shifts the Fermi level of the NPs. When the generation of hot carriers and their partial quenching reach a steady state under continuous irradiation (photostationary state), the number of accumulated ground state carriers on the particle will reach a constant value and the Fermi level of the particles reaches a new steady-state value. This new value corresponds to a new redox potential of the photo-charged NPs. Since the lifetime of the hot carriers is only a few picoseconds,[27] the photocatalysts maintain the net charges at the ground state during the course of the catalysis. Therefore, the photocatalysts will eventually reach photostationary-state redox potentials under continuous irradiation, and these potentials can be measured by establishing chemical equilibria between the catalysts and a known redox couple. Here, we show that the degree of hot hole quenching can be manipulated by changing the wavelength of the absorbed photons. Thus, the Fermi level and the redox potential can be tuned. The shift of Fermi level through selective quenching of one type of hot carriers (electrons or holes) has been demonstrated for AuNPs[28-31] and semiconductor-metal composites.[32, 33] However, the redox potentials of the photo-charged NP catalysts have not been measured despite the fact that they are important metrics for predicting which reactions can be catalyzed. We anticipate that the photo-tuning of the redox potential will open a way to tune the photocatalytic activities and selectivities of metallic NP photocatalysts. It is also worth mentioning that the photo-charged NPs work as the

catalysts when they are at the ground state. Hence, they have much longer time to catalyze a reaction than previously studied metallic NP photocatalysts where their activities are limited by the short lifetime of the hot carriers.

In this report, we determined the redox potentials of colloidal AuNPs at photostationary states under photo-irradiation with various wavelengths. The photoinduced oxidative etching of AuNPs by iron(III) chloride (Figure 8) was allowed to proceed until photostationary states were reached. UV-Vis spectroscopy and chemical assays were used to determine the concentrations of reactants and products at equilibrium. The photoredox potential of the particles can then be calculated using the Nernst equation. Based on our observations, the photoredox potential of the AuNPs decreases as the excitation wavelength decreases, which corresponds to a Fermi level rise.[28, 34] We found that the photoredox potential of the AuNP catalysts in our experiment can be tuned to a range of 1.28 to 1.40 V (vs. SHE) under irradiation in the wavelength range of 450 to 517 nm. These photoredox potentials are much lower than the potential of 1.48 V for particles under the non-irradiation condition.

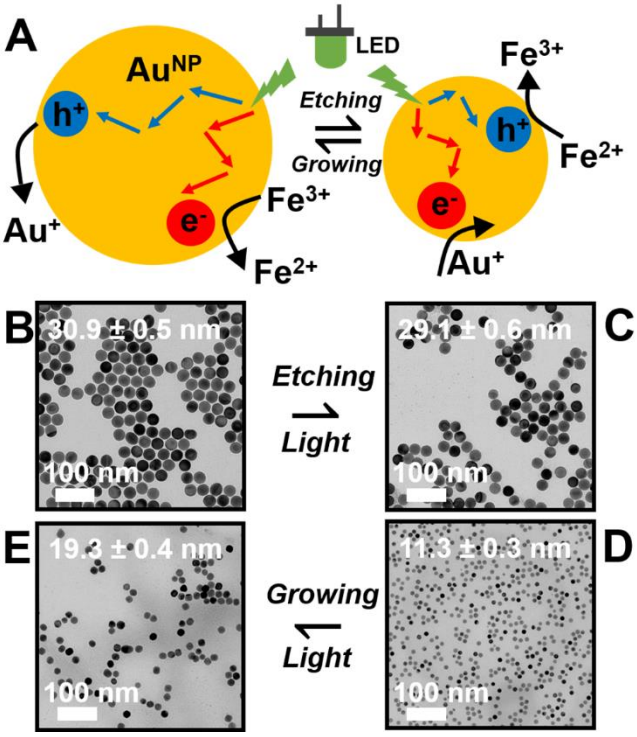

Figure 8. Reaction scheme and representative TEM images of colloidal AuNP catalysts in this study. (A) Scheme of oxidative etching (forward reaction) and growth (reverse reaction) of spherical AuNPs under photocatalyzed condition. (B and C) TEM images of a representative sample before and after the etching reaction reaches equilibrium under 490 nm light irradiation. (D and E) TEM images of another sample before and after the growth reaction reaches equilibrium under 490 nm light irradiation. Reprinted with permission from Ref.[35] Copyright 2020 American Chemical Society.

Results

The kinetics of photo-catalyzed etching reaction of AuNPs by iron(III) chloride has been studied previously.[15, 17] In this experiment, we observed the reaction at much longer time scale until the kinetic traces stopped changing. Figure 8 shows the scheme of the forward and reverse reactions as well as the electron micrographs of representative samples before and after reactions. To prevent the direct photoreduction of iron(III)[36] that could interfere with our studied reactions, a longpass filter with a cut-off wavelength of 446 nm was inserted in front of each LED because iron(III) ions absorb from the ultraviolet to around 440 nm.

The reaction kinetics of the forward reaction under irradiation of four different wavelengths and the non-irradiation condition are contrasted in Figure 9. In the etching experiments, three AuNP samples with average diameters of 30.9, 32.8 or 34.9 nm were used. This size variation is due to the small-batch synthesis method that we adopted to obtain NPs with highly narrow size and shape distributions.[37] In these kinetic measurements, only excitation wavelengths are changed. It is clear that the etching reactions, as represented by the decrease of the LSPR peak at around 525 nm, slow down over time and eventually approach steady states. These reactions are now considered to approach equilibria at long time scales. The equilibria shifted more to the product side when the reactions are photocatalyzed. The equilibrium was further confirmed by the fact that the reaction started to shift back to the reactants slowly (indication of particle re-growth) after blocking the light (Figure 17). When shorter wavelength light was used, the reactions reached equilibria faster, which is in agreement with our previous studies that the reaction was catalyzed faster by interband excitation rather than by plasmon excitation.[15, 17] The most interesting result here is that the equilibria shift further to the product side as shorter wavelength photons were used.

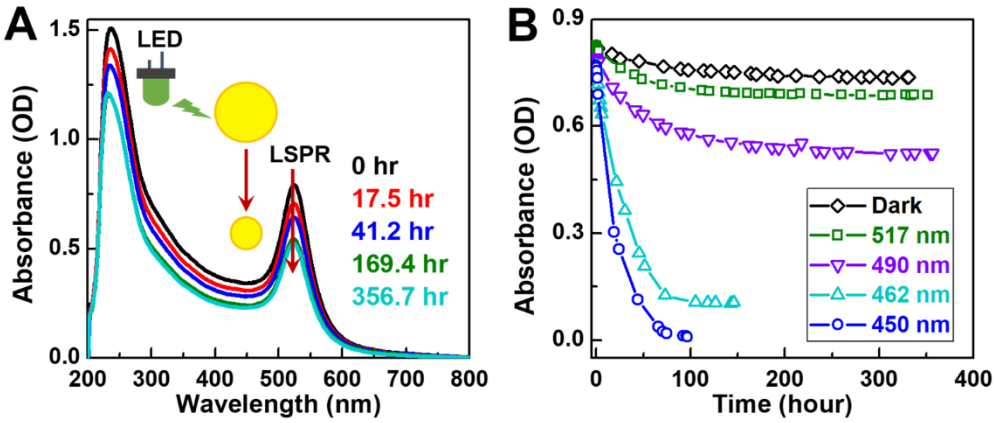

Figure 9. Kinetic study of the photo-catalyzed etching of colloidal AuNPs by iron(III) chloride. (A) Representative absorption spectra at different irradiation time points for the oxidative etching reaction under 490 nm light excitation. (B) Representative reaction kinetics as monitored by the LSPR peak of AuNPs under the dark and under light irradiation with wavelength of 450 nm (incident power: 111 mW), 462 nm (111 mW),

490 nm (100 mW), and 517 nm (100 mW). Reprinted with permission from Ref.[35] Copyright 2020 American Chemical Society.

To further prove that the above reactions are reversible and indeed can reach equilibria, the reaction was carried out in the reverse direction. The reactants started as 11.3 nm AuNPs (Figure 8D), gold(I) chloride, and iron(II) chloride in CTAB solutions (See the Methods section for details). The reactions were conducted under the same irradiation conditions as their forward reaction counterparts. Figure 10 shows the representative spectra at select time points and the kinetics of the reverse reaction under 490 nm irradiation. The LSPR band of the AuNPs increased over time and eventually stopped changing when the particles grew to an average diameter of 19.3 nm (Figure 8E). Reverse reactions under other wavelengths and under non-irradiation condition showed similar growing processes (See Figure 18 and 19). The NP products of the reverse reactions at equilibria tend to have more non-spherical shapes and wider size distributions probably because the reaction condition is very different from that of common NP growing procedures[37] (Figures 18 and 19). Due to this high degree of irregular growth, the equilibrium points were observed to have high experimental errors. Therefore, the reverse reaction data were not used for the redox potential calculations.

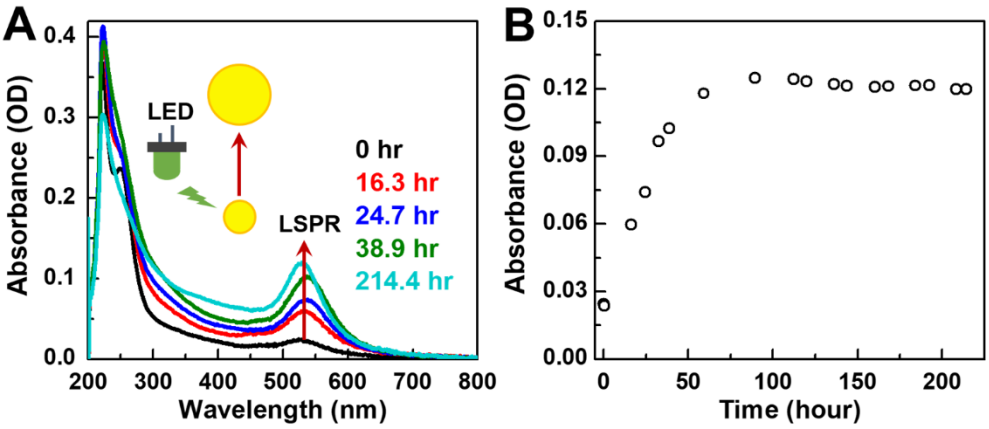

Figure 10. Kinetics of photo-catalyzed growth reaction of 11.3 nm AuNPs under irradiation of 490 nm light at the incident power of 100 mW. (A) Representative spectra at select time points of irradiation. (B) Reaction kinetics monitored at the LSPR peak in A. Reprinted with permission from Ref.[35] Copyright 2020 American Chemical Society.

Once the reactions reach equilibria, the amount of gold etched can be calculated based on the change of the LSPR peak because the molar absorption coefficient of gold nanospheres at the LSPR peak is approximately proportional to the third power of their radius.[17, 38] Chemical assays confirmed that all gold ions exist in the form of gold(I) in the reaction mixture at equilibrium, presumably the gold(III) ions that formed in the intermediate step further reacted with the NPs and became gold(I) (See Supporting Information and Figure 16). Therefore, the amount of gold etched is equal to the amount of gold(I) ions in the equilibrium reaction solution. The concentration of iron(II) in the reaction mixtures can be determined through the phenanthroline assay[39] (See Supporting Information). The concentrations of other chemical substances in the equilibrium reaction

mixtures can be obtained based on the concentrations of gold(I) and iron(II). Since the concentrations of all the chemical substances at equilibrium are in the sub-millimolar range, the activity coefficients are close to 1 and concentrations were used instead of activities in the calculation of the redox potentials. The redox potential of the AuNPs, $\left[E^0_{Au^+/Au}\right]^{NP_n}$, can then be calculated using the Nernst equation. Here, *n* denotes the number of gold atoms in each AuNP. Since there are no gold(III) ions in the equilibrium reaction solution, the chemical equations can be written as:

$$AuNP_n + Fe^{3+} \rightleftharpoons AuNP_{n-1} + Au^+ + Fe^{2+} \quad (1)$$

$$Au^+ + 2Br^- \rightleftharpoons AuBr_2^- \quad (2)$$

All Au^+ ions are assumed to exist as $AuBr_2^-$ because the concentration of bromide ions (1.1 mM) added to the reaction mixture is several times higher than that of Au^+ ions (< 0.2 mM) and the stability constant of $AuBr_2^-$ is very high:[40]

$$\beta = \frac{[AuBr_2^-]}{[Au^+][Br^-]^2} = 10^{12} M^{-2} \quad (3)$$

For simplicity, the influence of the chloride complexes of Au^+ was ignored because the stability constant of $AuBr_2^-$ is three orders of magnitude higher than that of $AuCl_2^-$.[40] At equilibrium, the cell potential for chemical reaction (1) will be zero:

$$E_{cell} = E^0_{Fe^{3+}/Fe^{2+}} - \left[E^0_{Au^+/Au}\right]^{NP_n} - \frac{RT}{F} ln \frac{[Au^+][Fe^{2+}]}{[Fe^{3+}]} = 0 \quad (4)$$

where R is the ideal gas constant, T is temperature, and F is the Faraday constant.

Substitute equation (3) into equation (4):

$$E_{cell} = E^0_{Fe^{3+}/Fe^{2+}} - \left[E^0_{Au^+/Au}\right]^{NP_n} - \frac{RT}{F} ln \frac{[AuBr_2^-][Fe^{2+}]}{\beta[Br^-]^2[Fe^{3+}]} = 0 \quad (5)$$

Therefore,

$$\left[E^0_{Au^+/Au}\right]^{NP_n} = E^0_{Fe^{3+}/Fe^{2+}} - \frac{RT}{F} ln \frac{[AuBr_2^-][Fe^{2+}]}{\beta[Br^-]^2[Fe^{3+}]} \quad (6)$$

The calculated standard redox potentials for AuNPs, $\left[E^0_{Au^+/Au}\right]^{NP_n}$, under different irradiation conditions are summarized in Table 2 and plotted in Figure 11. The standard redox potential under the non-irradiation condition is lower than the bulk value (1.83 V vs SHE).[41] This is consistent with theoretical predictions and previous experimental studies where metallic NPs were found to have lower redox potential than bulk metals.[42-44] Interestingly, the redox potential decreases as the irradiation wavelength decreases. The redox potential $\left[E^0_{AuBr_2^-/Au}\right]^{NP_n}$ was also calculated (See Supporting Information, Table 2, and Figure 20) and showed the same trend as $\left[E^0_{Au^+/Au}\right]^{NP_n}$. A very similar change was also observed for a sample of smaller size (11.3 nm average diameter,

see Figure 21 and Table 3) which implies that the influence of NP size to the redox potential is negligible when the size changes within the range of about 10 to 30 nm. The half-cell potential of each reaction was calculated as well and showed the same wavelength dependent trend (Figure 22).

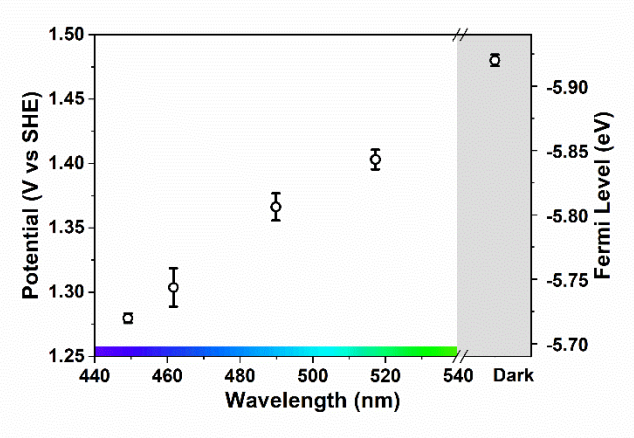

Figure 11. Wavelength dependence of the standard redox potential $\left[E^0_{Au^+/Au}\right]^{NP_n}$ of AuNPs under photoexcitation at the incident power of ~100 mW, compared with non-irradiation condition (shaded area). Experimental uncertainty is reported as one standard error. The right vertical axis shows the Fermi level (E_{Fermi}) corresponding to the redox potential relative to the vacuum level: $E_{Fermi}(\text{eV}) = -4.44\ \text{eV} - e \cdot E_{redox}(\text{V vs SHE})$.[45] Reprinted with permission from Ref.[35] Copyright 2020 American Chemical Society.

With regard to the influence of the optical power to the redox potential, we found that the redox potential tends to decrease as power increases (Figure 23, 24, and Table 4). At various excitation wavelengths, the decrease of photoredox potential was between 0.02–0.08V when the incident power increased within the range of 10 mW to 190 mW. This trend is consistent with the report by Jain et al. where higher optical power leads to a larger accumulation of hot electrons on polyvinylpyrrolidone (PVP) stabilized AuNPs.[28] The accumulation of electrons on gold NPs was proposed to raise the quasi-Fermi level,[28] which is equivalent to lowering the photoredox potential.

Discussions

As we expected, the redox potentials at photostationary states are different from the redox potential under non-photoexcitation. The decrease in the redox potential at the photostationary state must come from the rise of the Fermi level, which is a result of accumulation of electrons on the particles. This result can only be explained by the fact that the quenching of hot holes through oxidative etching of the gold atoms is faster than the quenching of hot electrons by iron(III). Some of the hot electrons and the accumulated ground state electrons on the particles are scavenged by iron(III) in the solution, but the accumulation of electrons will eventually reach a photostationary state where the particles are charged at the ground state. As the photocatalyzed reactions proceed to the photostationary state, the electrochemical reactions between the two haft

cells, gold(I)/gold(0)$_{NP}$ and iron(III)/iron(II) will reach an equilibrium, and the photo-charged particles will reach a steady-state photoredox potential. Briefly, photoexcitation and hole quenching are utilized to charge the AuNPs, but their catalytic activity increases due to a decrease in redox potential at the ground state.

The wavelength dependence of the redox potential is somewhat surprising but not contradictory to the literature. In the ferricyanide-to-ferrocyanide reduction reaction catalyzed by colloidal AuNPs under 488 nm photoexcitation at around 500 mW, Jain et al. estimated a rise of the Fermi level or a built-up photoelectrochemical potential up to 240 mV in the AuNPs compared to the Fermi level of bulk gold under non-photoirradiation condition.[28] They also observed that the rise of the quasi-Fermi level under interband excitation using a 488 nm laser is larger than that under plasmon excitation using a 514.5 nm laser. The data support their argument that the built-up photoelectrochemical potential effectively reduces the activation energy of the ferricyanide-to-ferrocyanide reaction. In electrochemical cells made by Ag or Au NPs adsorbed on electrodes,[29, 30] quenching the hot holes by oxidizing citrate ligands on the particles results in a cathodic photovoltage under open circuit in the cell. The photovoltage increases with increasing photon energy due to the more effective quenching of deeper *d*-band holes generated under photoexcitation of higher energy photons. All of these previous works pave the way for this study: the photostationary-state redox potential of the NP photocatalysts can be tuned by changing the excitation wavelength.

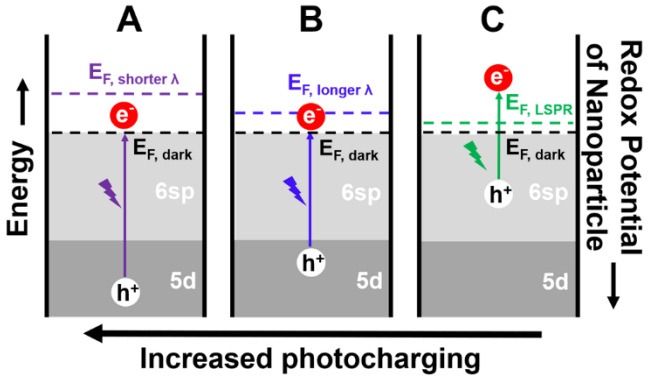

Figure 12. Scheme illustrating the wavelength dependence of the redox potential at photostationary states under photoexcitation of different wavelengths. (A) Interband excitation using shorter (purple) wavelength light. (B) Interband excitation using longer (blue) wavelength light. (C) Plasmon excitation (olive). The energy on the left axis is relative to the vacuum level. Reprinted with permission from Ref.[35] Copyright 2020 American Chemical Society.

As for the wavelength dependence of the photoredox potentials under the interband excitations at 450 nm, 462 nm and 490 nm (Fig. 4), it can be attributed to the difference in the energy of the hot holes generated by photons of different energy. It is known that interband excitation promotes the transition of electrons from the *d* band to the *sp* band of the metal and the hot electrons reside close to the Fermi level. Higher energy photons generate hot holes that are deeper in the *d* band and are more oxidizing

(Figure 12 A vs B). These highly oxidizing hot holes will be quenched by oxidizing gold atoms to form gold(I) complexes more easily, which leads to the accumulation of more electrons on the AuNPs. The accumulation of more electrons will lead to a larger rise of the Fermi level and a larger decrease of the redox potential of the AuNPs, as illustrated by Figure 12. As for the LSPR excitation by 517 nm light, the hole quenching is not as efficient as under interband excitation,[15, 17] so a smaller decrease of redox potential was observed.

The AuNP etching products end up to different sizes at different equilibria as seen by the LSPR absorbance (Fig. 2B) and TEM. The equilibrium sizes are smaller for shorter wavelength excitations, which raises concerns about the influence of particle size on the calculated redox potential. There are two main concerns as the particles get smaller: the decrease in the number of absorbed photons and the reduction of redox potential. As mentioned in the results section, the decrease of absorbed photons, equivalent to reducing the optical power of the incident light, slightly increases the photoredox potential. This effect is very small within the range of change of absorbed optical power across different wavelengths in this study compared to the wavelength-dependent effect seen in Figure 11, thus it is not a concern. To address the size effect on the redox potential, we refer to the size dependence of redox potential of metallic NPs under non-photoexcited condition in previous theoretical studies[46] because the photoredox potential is calculated for the ground state of the particles in our experiment. This value can be estimated by considering the change of free energy associated with the change in surface area according to the following equation:[42, 46]

$$\left[E^0_{M^+/M}\right]^{NP_n} = \left[E^0_{M^+/M}\right]^{bulk} - \frac{2\Upsilon V_m}{F}\left(\frac{1}{r}\right)$$

where Υ is the surface tension of metal *M*, V_m is the molar volume of the metal, *F* is the Faraday constant, *r* is the radius of the NPs.

Take the etching reaction of 34.9 nm AuNPs at 490 nm (100 mW) as an example, the average size of the AuNPs at equilibrium is 23.9 nm, whereas the size of the AuNPs at equilibrium under non-irradiation etching condition is 32.0 nm. According to the above equation, the change of redox potential due to a size decrease of 8.1 nm is 8.37 mV, which is small compared to the experimentally observed redox potential change (114 mV) due to photoirradiation. The details of calculation according to the above equation along with the size effect under photoexcitation of other wavelengths are discussed further in the supporting information.

The accumulation of electrons on the NPs will also have an influence on the above calculation of size effect on the redox potential. Due to our experimental limitation, the actual number of accumulated electrons could not be determined (see SI). Nevertheless, the size effect to the redox potential is very small and does not differ much whether the accumulated electrons on the particles were considered or not, as is discussed in the supporting information and Table 1. Taking the above example of etching 34.9 nm AuNPs at 490 nm (100 mW), and assuming each particle has accumulated an imaginarily

large number of electrons (such as 500 electrons), the reduction of redox potential due to a size decrease of 8.1 nm is 8.47 mV. This value is close to 8.37 mV when no electrons were assumed to have accumulated on the NPs. Thus, these arguments support our conclusion that the observed reduction of redox potentials is not due to the reduction of the particle size during our etching reaction. In fact, the redox potentials that we observed for the etching of ~30 and ~ 11 nm AuNPs were in the same range (Fig 4 and Fig S7). Taken together, the observed wavelength dependence of the redox potentials is mainly due to the larger number of electrons accumulated on the NPs when shorter wavelength photons were used, and not because of the smaller size of the NPs at equilibria.

The rise of local temperature around the NPs could affect the catalytic activities.[47] Under our experimental condition, the heat dissipation of the colloidal particles is very effective and the average rise of temperature for each NP after a single photon absorption is negligible, thus the local temperature has a negligible effect on the observed catalysis.[15, 48] The rise of the solution temperature in our experiment is also neglectable, thus heating has no effect on the calculated redox potential.

Lastly, we anticipate that our strategy of tuning the redox potential of metallic NPs through photo-charging can be applied widely in many other chemical reactions. In our experiment, we choose to quench the hot holes by etching the AuNP photocatalysts because the reaction can be conveniently studied by monitoring the optical spectra of AuNPs. Other hole quenchers, such as ethanol[28] or citrate ligands,[29, 49] have been successfully used without etching the AuNP photocatalysts. We envision that many other hole or electron quenchers can be used to tune the charge (hence the redox potential and the photocatalytic performance) of metallic NP photocatalysts.

Conclusions

The photoredox potential of AuNP photocatalysts at the photostationary state was determined under irradiation with various wavelengths. The potential decreases significantly when shorter wavelength light was used. The deeper *d*-band hot holes generated under shorter wavelength irradiation was proposed to contribute to the observed wavelength dependence of the photoredox potential. Our results demonstrate the tunability of photoredox potential of metallic NPs which predictably affects the photocatalytic activities and selectivities. The ability to tune metallic NPs' catalytic activities and selectivities through light has potential applications in chemical synthesis, especially for electron transfer reactions, and solar energy harvesting.

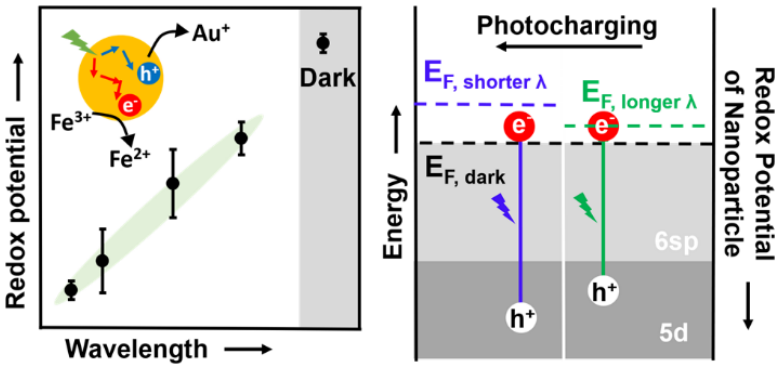

Figure 13. The wavelength-dependent shift in the reduction potential is due to the photocharging effect. Under photoexcitation, the holes oxidize the AuNPs, leading to the accumulation of ground state electrons. This accumulation raises the Fermi level or lowers the AuNP reduction potentials. Shorter wavelengths generate deeper holes, which lead to greater photocharging and a larger shift in potential. Reprinted with permission from Ref.[35] Copyright 2020 American Chemical Society.

Ch. 3 – References

(1) Aslam, U.; Rao, V. G.; Chavez, S.; Linic, S. Catalytic conversion of solar to chemical energy on plasmonic metal nanostructures. *Nature Catalysis* **2018**, *1* (9), 656-665. DOI: 10.1038/s41929-018-0138-x.
(2) Zhou, L. A.; Swearer, D. F.; Zhang, C.; Robatjazi, H.; Zhao, H. Q.; Henderson, L.; Dong, L. L.; Christopher, P.; Carter, E. A.; Nordlander, P.; et al. Quantifying hot carrier and thermal contributions in plasmonic photocatalysis. *Science* **2018**, *362* (6410), 69-+. DOI: 10.1126/science.aat6967.
(3) Christopher, P.; Moskovits, M. Hot Charge Carrier Transmission from Plasmonic Nanostructures. *Annual Review of Physical Chemistry* **2017**, *68* (1), 379-398. DOI: 10.1146/annurev-physchem-052516-044948.
(4) Seemala, B.; Therrien, A. J.; Lou, M.; Li, K.; Finzel, J. P.; Qi, J.; Nordlander, P.; Christopher, P. Plasmon-Mediated Catalytic O2 Dissociation on Ag Nanostructures: Hot Electrons or Near Fields? *ACS Energy Letters* **2019**, 1803-1809. DOI: 10.1021/acsenergylett.9b00990.
(5) Chang, L.; Besteiro, L. V.; Sun, J. C.; Santiago, E. Y.; Gray, S. K.; Wang, Z. M.; Govorov, A. O. Electronic Structure of the Plasmons in Metal Nanocrystals: Fundamental Limitations for the Energy Efficiency of Hot Electron Generation. *ACS Energy Letters* **2019**, *4* (10), 2552-2568. DOI: 10.1021/acsenergylett.9b01617.
(6) DuChene, J. S.; Tagliabue, G.; Welch, A. J.; Cheng, W.-H.; Atwater, H. A. Hot Hole Collection and Photoelectrochemical CO2 Reduction with Plasmonic Au/p-GaN Photocathodes. *Nano Lett.* **2018**, *18* (4), 2545-2550. DOI: 10.1021/acs.nanolett.8b00241.
(7) Kim, Y.; Smith, J. G.; Jain, P. K. Harvesting multiple electron-hole pairs generated through plasmonic excitation of Au nanoparticles. *Nature Chemistry* **2018**, *10* (7), 763-769. DOI: 10.1038/s41557-018-0054-3.
(8) Zhang, Y.; He, S.; Guo, W.; Hu, Y.; Huang, J.; Mulcahy, J. R.; Wei, W. D. Surface-Plasmon-Driven Hot Electron Photochemistry. *Chemical Reviews* **2018**, *118* (6), 2927-2954. DOI: 10.1021/acs.chemrev.7b00430.
(9) Al-Zubeidi, A.; Hoener, B. S.; Collins, S. S. E.; Wang, W.; Kirchner, S. R.; Hosseini Jebeli, S. A.; Joplin, A.; Chang, W.-S.; Link, S.; Landes, C. F. Hot Holes Assist Plasmonic Nanoelectrode Dissolution. *Nano Lett.* **2019**, *19* (2), 1301-1306. DOI: 10.1021/acs.nanolett.8b04894.
(10) Huang, Y.; Liu, Z.; Gao, G.; Xiao, Q.; Martens, W.; Du, A.; Sarina, S.; Guo, C.; Zhu, H. Visible light-driven selective hydrogenation of unsaturated aromatics in an aqueous solution by direct photocatalysis of Au nanoparticles. *Catalysis Science & Technology* **2018**, *8* (3), 726-734, 10.1039/C7CY02291C. DOI: 10.1039/C7CY02291C.
(11) Kazuma, E.; Kim, Y. Mechanistic Studies of Plasmon Chemistry on Metal Catalysts. *Angewandte Chemie-International Edition* **2019**, *58* (15), 4800-4808. DOI: 10.1002/anie.201811234.
(12) Zhang, Z. L.; Zhang, C. Y.; Zheng, H. R.; Xu, H. X. Plasmon-Driven Catalysis on Molecules and Nanomaterials. *Accounts of Chemical Research* **2019**, *52* (9), 2506-2515. DOI: 10.1021/acs.accounts.9b00224.
(13) Yu, Y.; Wijesekara, K. D.; Xi, X.; Willets, K. A. Quantifying Wavelength-Dependent Plasmonic Hot Carrier Energy Distributions at Metal/Semiconductor Interfaces. *ACS Nano* **2019**, *13* (3), 3629-3637. DOI: 10.1021/acsnano.9b00219.

(14) Gellé, A.; Jin, T.; de la Garza, L.; Price, G. D.; Besteiro, L. V.; Moores, A. Applications of Plasmon-Enhanced Nanocatalysis to Organic Transformations. *Chemical Reviews* **2019**. DOI: 10.1021/acs.chemrev.9b00187.
(15) Zhao, J.; Nguyen, S. C.; Ye, R.; Ye, B. H.; Weller, H.; Somorjai, G. A.; Alivisatos, A. P.; Toste, F. D. A Comparison of Photocatalytic Activities of Gold Nanoparticles Following Plasmonic and Interband Excitation and a Strategy for Harnessing Interband Hot Carriers for Solution Phase Photocatalysis. *Acs Central Science* **2017**, *3* (5), 482-488, Article. DOI: 10.1021/acscentsci.7b00122.
(16) Zheng, B. Y.; Zhao, H.; Manjavacas, A.; McClain, M.; Nordlander, P.; Halas, N. J. Distinguishing between plasmon-induced and photoexcited carriers in a device geometry. *Nature Communications* **2015**, *6* (1), 7797. DOI: 10.1038/ncomms8797.
(17) Mao, Z.; Vang, H.; Garcia, A.; Tohti, A.; Stokes, B. J.; Nguyen, S. C. Carrier Diffusion—The Main Contribution to Size-Dependent Photocatalytic Activity of Colloidal Gold Nanoparticles. *ACS Catal.* **2019**, *9* (5), 4211-4217. DOI: 10.1021/acscatal.9b00390.
(18) Yu, Y.; Sundaresan, V.; Willets, K. A. Hot Carriers versus Thermal Effects: Resolving the Enhancement Mechanisms for Plasmon-Mediated Photoelectrochemical Reactions. *Journal of Physical Chemistry C* **2018**, *122* (9), 5040-5048. DOI: 10.1021/acs.jpcc.7b12080.
(19) Cortes, E. Efficiency and Bond Selectivity in Plasmon-Induced Photochemistry. *Advanced Optical Materials* **2017**, *5* (15). DOI: ARTN 1700191

10.1002/adom.201700191.
(20) Boerigter, C.; Campana, R.; Morabito, M.; Linic, S. Evidence and implications of direct charge excitation as the dominant mechanism in plasmon-mediated photocatalysis. *Nature Communications* **2016**, *7* (1), 10545. DOI: 10.1038/ncomms10545.
(21) Kale, M. J.; Avanesian, T.; Xin, H.; Yan, J.; Christopher, P. Controlling Catalytic Selectivity on Metal Nanoparticles by Direct Photoexcitation of Adsorbate–Metal Bonds. *Nano Lett.* **2014**, *14* (9), 5405-5412. DOI: 10.1021/nl502571b.
(22) Yan, L.; Wang, F. W.; Meng, S. Quantum Mode Selectivity of Plasmon-Induced Water Splitting on Gold Nanoparticles. *ACS Nano* **2016**, *10* (5), 5452-5458. DOI: 10.1021/acsnano.6b01840.
(23) Zhu, H. M.; Yang, Y.; Wu, K. F.; Lian, T. Q. Charge Transfer Dynamics from Photoexcited Semiconductor Quantum Dots. *Annual Review of Physical Chemistry* **2016**, *67*, 259-281. DOI: 10.1146/annurev-physchem-040215-112128.
(24) Yan, Y.; Crisp, R. W.; Gu, J.; Chernomordik, B. D.; Pach, G. F.; Marshall, A. R.; Turner, J. A.; Beard, M. C. Multiple Exciton Generation for Photoelectrochemical Hydrogen Evolution Reactions with Quantum Yields Exceeding 100%. *Nature Energy* **2017**, *2* (5). DOI: ARTN 17052

10.1038/nenergy.2017.52.
(25) Twilton, J.; Le, C.; Zhang, P.; Shaw, M. H.; Evans, R. W.; MacMillan, D. W. C. The Merger of Transition Metal and Photocatalysis. *Nature Reviews Chemistry* **2017**, *1* (7). DOI: UNSP 0052

10.1038/s41570-017-0052.

(26) Romero, N. A.; Nicewicz, D. A. Organic Photoredox Catalysis. *Chemical Reviews* **2016**, *116* (17), 10075-10166. DOI: 10.1021/acs.chemrev.6b00057.
(27) Minutella, E.; Schulz, F.; Lange, H. Excitation-Dependence of Plasmon-Induced Hot Electrons in Gold Nanoparticles. *Journal of Physical Chemistry Letters* **2017**, *8* (19), 4925-4929. DOI: 10.1021/acs.jpclett.7b02043.
(28) Kim, Y.; Torres, D. D.; Jain, P. K. Activation Energies of Plasmonic Catalysts. *Nano Lett.* **2016**, *16* (5), 3399-3407. DOI: 10.1021/acs.nanolett.6b01373.
(29) Thrall, E. S.; Steinberg, A. P.; Wu, X. M.; Brus, L. E. The Role of Photon Energy and Semiconductor Substrate in the Plasmon-Mediated Photooxidation of Citrate by Silver Nanoparticles. *Journal of Physical Chemistry C* **2013**, *117* (49), 26238-26247. DOI: 10.1021/jp409586z.
(30) Schlather, A. E.; Manjavacas, A.; Lauchner, A.; Marangoni, V. S.; DeSantis, C. J.; Nordlander, P.; Halas, N. J. Hot Hole Photoelectrochemistry on Au@SiO2@Au Nanoparticles. *The Journal of Physical Chemistry Letters* **2017**, *8* (9), 2060-2067. DOI: 10.1021/acs.jpclett.7b00563.
(31) Wilson, A. J.; Mohan, V.; Jain, P. K. Mechanistic Understanding of Plasmon-Enhanced Electrochemistry. *The Journal of Physical Chemistry C* **2019**, *123* (48), 29360-29369. DOI: 10.1021/acs.jpcc.9b10473.
(32) Subramanian, V.; Wolf, E. E.; Kamat, P. V. Green Emission to Probe Photoinduced Charging Events in ZnO-Au Nanoparticles. Charge Distribution and Fermi-Level Equilibration. *Journal of Physical Chemistry B* **2003**, *107* (30), 7479-7485. DOI: 10.1021/jp0275037.
(33) Subramanian, V.; Wolf, E. E.; Kamat, P. V. Catalysis with TiO2/Gold Nanocomposites. Effect of Metal Particle Size on the Fermi Level Equilibration. *Journal of the American Chemical Society* **2004**, *126* (15), 4943-4950. DOI: 10.1021/ja0315199.
(34) Reiss, H. The Fermi level and the redox potential. *The Journal of Physical Chemistry* **1985**, *89* (18), 3783-3791. DOI: 10.1021/j100264a005.
(35) Mao, Z.; Espinoza, R.; Garcia, A.; Enwright, A.; Vang, H.; Nguyen, S. C. Tuning Redox Potential of Gold Nanoparticle Photocatalysts by Light. *ACS Nano* **2020**, *14* (6), 7038-7045. DOI: 10.1021/acsnano.0c01704.
(36) Bates, H. G. C.; Uri, N. Oxidation of Aromatic Compounds in Aqueous Solution by Free Radicals Produced by Photo-Excited Electron Transfer in Iron Complexes. *Journal of the American Chemical Society* **1953**, *75* (11), 2754-2759. DOI: DOI 10.1021/ja01107a062.
(37) Zheng, Y. Q.; Zhong, X. L.; Li, Z. Y.; Xia, Y. N. Successive, Seed-Mediated Growth for the Synthesis of Single-Crystal Gold Nanospheres with Uniform Diameters Controlled in the Range of 5-150 nm. *Particle & Particle Systems Characterization* **2014**, *31* (2), 266-273. DOI: 10.1002/ppsc.201300256.
(38) Near, R. D.; Hayden, S. C.; Hunter, R. E.; Thackston, D.; El-Sayed, M. A. Rapid and Efficient Prediction of Optical Extinction Coefficients for Gold Nanospheres and Gold Nanorods. *The Journal of Physical Chemistry C* **2013**, *117* (45), 23950-23955. DOI: 10.1021/jp4082596.
(39) Saywell, L. G.; Cunningham, B. B. Determination of Iron: Colorimetric o-Phenanthroline Method. *Industrial & Engineering Chemistry Analytical Edition* **1937**, *9* (2), 67-69. DOI: 10.1021/ac50106a005.

(40) Nicol, M. J.; Fleming, C. A.; Paul, R. L. The chemistry of the extraction of gold. In *The Extractive Metallurgy of Gold in South Africa*, Stanley, G. G. Ed.; Vol. Chapter 15; South African Institute of Mining and Metallurgy, 1987; pp 831-906.
(41) Zou, R.; Guo, X.; Yang, J.; Li, D.; Peng, F.; Zhang, L.; Wang, H.; Yu, H. Selective etching of gold nanorods by ferric chloride at room temperature. *CrystEngComm* **2009**, *11* (12), 2797-2803, 10.1039/B911902G. DOI: 10.1039/B911902G.
(42) Scanlon, M. D.; Peljo, P.; Méndez, M. A.; Smirnov, E.; Girault, H. H. Charging and discharging at the nanoscale: Fermi level equilibration of metallic nanoparticles. *Chem. Sci.* **2015**, *6* (5), 2705-2720, 10.1039/C5SC00461F. DOI: 10.1039/C5SC00461F.
(43) Al-Zubeidi, A.; Hoener, B. S.; Collins, S. S. E.; Wang, W. X.; Kirchner, S. R.; Jebeli, S. A. H.; Joplin, A.; Chang, W. S.; Link, S.; Landes, C. F. Hot Holes Assist Plasmonic Nanoelectrode Dissolution. *Nano Letters* **2019**, *19* (2), 1301-1306. DOI: 10.1021/acs.nanolett.8b04894.
(44) Masitas, R. A.; Zamborini, F. P. Oxidation of Highly Unstable <4 nm Diameter Gold Nanoparticles 850 mV Negative of the Bulk Oxidation Potential. *Journal of the American Chemical Society* **2012**, *134* (11), 5014-5017. DOI: 10.1021/ja2108933.
(45) Haram, S. K. Semiconductor Electrodes. In *Handbook of Electrochemistry*, Zoski, C. G. Ed.; Elsevier, 2007; p 342.
(46) Plieth, W. J. Electrochemical properties of small clusters of metal atoms and their role in the surface enhanced Raman scattering. *The Journal of Physical Chemistry* **1982**, *86* (16), 3166-3170. DOI: 10.1021/j100213a020.
(47) Sivan, Y.; Baraban, J.; Un, I. W.; Dubi, Y. Comment on "Quantifying Hot Carrier and Thermal Contributions in Plasmonic Photocatalysis". *Science* **2019**, *364* (6439). DOI: ARTN eaaw9367

10.1126/science.aaw9367.
(48) Nguyen, S. C.; Zhang, Q.; Manthiram, K.; Ye, X. C.; Lomont, J. P.; Harris, C. B.; Weller, H.; Alivisatos, A. P. Study of Heat Transfer Dynamics from Gold Nanorods to the Environment via Time-Resolved Infrared Spectroscopy. *ACS Nano* **2016**, *10* (2), 2144-2151. DOI: 10.1021/acsnano.5b06623.
(49) Schlather, A. E.; Manjavacas, A.; Lauchner, A.; Marangoni, V. S.; DeSantis, C. J.; Nordlander, P.; Halas, N. J. Hot Hole Photoelectrochemistry on Au@SiO_2@Au Nanoparticles. *J. Phys. Chem. Lett.* **2017**, *8* (9), 2060-2067. DOI: 10.1021/acs.jpclett.7b00563.

Ch. 4 Conclusion and Outlook

Conclusion

To conclude this body of work, the standard redox potentials of NPs can be determined using the Galvanic equilibration method. Galvanic equilibration is a powerful method that can be used to investigate the electrochemical properties of colloidal NPs that are otherwise challenging through other means. In a Galvanic equilibration reaction, the NPs are coupled to a redox probe that, once at equilibrium, the standard Gibbs free energy of the reaction or the standard reduction potential of the reaction can be determined. This approach has allowed us to investigate many physical and chemical factors that influence the reduction potential of NPs, such as light excitation, size, and local environment.

For metallic NPs, particle size was shown to be a major contributor to their reduction potential. This size trend was demonstrated by synthesizing spherical AuNPs with precise diameters and allowing them to undergo galvanic equilibration with the $Fe^{3+/2+}$ redox couple. Each size yielded different equilibrium constants, and by using the Nernst equation, the reduction potentials were determined. These reduction potentials were shown to follow the theoretical trends predicted by Plieth. In general, the shift in reduction potentials followed an inverse radius trend, decreasing from 0.248 V to 0.311 V for diameters from 74 nm to 4.4 nm, respectively.

Furthermore, this approach makes it possible to investigate the local environmental effects. We found that the CTA^+ surfactant acts as a stabilizer and lowers the standard reduction potentials. Additionally, the surfactant micelles were shown to play a critical kinetic role in the reaction. In the absence of the micelle, the galvanic reactions were kinetically sluggish.

Under photoexcitation, the AuNPs were demonstrated to possess different reduction potentials using the same techniques. Since the galvanic equilibration technique preserves the colloidal integrity of the particles, in practical terms, the photon efficiency can be easily measured as a function of incident power and wavelength. Our approach determined the reduction potentials to shift negatively with shorter excitation wavelengths, as shown as a decrease from 1.403 mV to 1.280 mV for the $Au^{+/0}$ couple when excited at 490 nm and 450 nm, respectively. This shift was induced by the photocharging in the AuNPs after being irradiated by light in the presence of Fe^{3+}. Photocharging raises the Fermi level due to the accumulation of electrons.

These examples demonstrate the versatility of the galvanic equilibration of the AuNPs to determine the reduction potentials. This technique's main advantage is measuring the standard reduction potentials of colloidal NPs.

Outlook

As discussed previously, galvanic equilibration was used to investigate the electrochemical properties of AuNPs in relation to electronic excitation, size, and local environment. However, this approach can potentially be adapted to other NPs with different elemental compositions, including non-metals, and dimensions. One avenue of interest is exploring how the crystallographic shape of NP affects the reductions potentials.

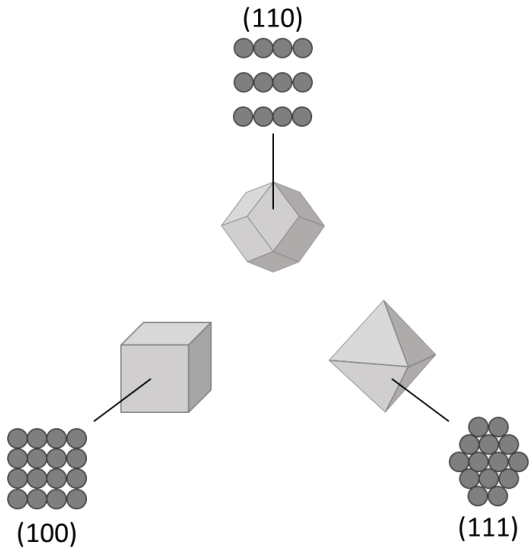

Figure 14. Scheme illustrating the crystallographic shapes of monofaceted NPs. For a face centered cubic crystal lattice, (100), (110), and (111) facets will yield cubes, rhombic dodecahedron, and octahedron nanocrystals, respectively. According to Plieth's equation, each of these nanocrystals should possess different reduction potentials due to the differences in surface tension.

The shape of the NP is especially important in terms of catalytic applications.[1, 2] In catalysis, the adsorption/desorption dynamics of the adsorbates depend on the atomic arrangement at the surface, or facets. Since NPs with different crystallographic shapes are composed of one or more surface facets, different shapes will possess unique catalytic activities. This is also true for the electrochemical stability of metallic NPs.

NPs possessing different crystallographic features will have different reduction potentials. Recall that Plieth's equation relates the size to not only the reduction potentials but also factors in the surface tension of the NP. The surface tension of these NPs is determined by their facets, which vary amongst different crystallographic shapes. Thus, the reduction potentials of various shapes can be determined from their overall surface tension. However, calculating the surface tension of complex shapes containing multiple facets may not be straight forward.

Furthermore, non-spherical NPs possess corners and edges with different surface tensions that complicate theoretical interpretations. Deconvoluting these factors may pose a serious technical challenge. Nonetheless, Galvanic equilibration is a potentially

powerful technique that can be broadly implemented to better understand the electrochemical and catalytic properties of colloidal nanomaterials.

Appendix 1 – Ch. 2 Methods

Chemicals and Materials

All purchased reagents were used without any further purification unless otherwise stated. L-Ascorbic acid (AA, >99%), gold(III) chloride trihydrate (HAuCl4·3H2O, 99.995%), 1,10-phenanthroline (PT, ≥99%), and sodium borohydride (NaBH4, 99.99%) were purchased form Sigma-Aldrich. Ammonium iron(II) sulfate hexahydrate ((NH4)2Fe(SO4)2·6H2O, 99%), cetyltrimethylammonium bromide (CTAB, >98.0%), and cetyltrimethylammonium chloride (CTAC, >95.0%) were purchased from Tokyo Chemical Industry Co., Ltd. Iron(III) chloride hexahydrate (FeCl3·6H2O, 99+%) and hydroxylamine hydrochloride (NH2OH·HCl, 99+%) were purchased from Acros. Hydrochloric acid (HCl, 36.5%, 99.999% trace metal basis) was purchased from Alfa Aesar. Acetic acid (99.9%) and sodium acetate (≥99.7%) were purchased from Fisher Scientific. All water used for the synthesis of the AuNPs and etching reactions was purified using the Milli-Q IQ7000 system. [copy paste from ACS Nano 2020]

Instrumentation

The synthesized gold nanospheres were characterized using a FEI TALOS F200C G2 transmission electron microscope (TEM) operated at 200 kV. The reaction kinetics were monitored using UV−vis spectrometers (Ocean Optics, Maya 2000 Pro or USB 4000). The reaction mixtures were prepared in 1 cm path length quartz cuvettes from Spectrocell (R- 3010-T). Caps with an opening on top were used to seal the cuvettes with rubber septa. The samples were then purged using nitrogen gas on a Schlenk line to get rid of oxygen.

AuNP seed-mediated synthesis

The AuNPs used in this study were synthesized by following the procedures reported by Zheng and coworkers except that the volumes were scaled up by 20 times to obtain more particles per synthesis.[3] For the largest AuNPs (74 nm), the procedure was slightly modified following the procedures reported by Lee and coworkers to obtain consistent size and shape distributions.[4]

Etching Reactions of AuNPs by $FeCl_3$

In a 1 cm path length cuvette, aliquots of AuNPs in 20 mM CTAC were injected into a solution containing 0.267 mM $FeCl_3$ and 1.1 mM CTAC, and brought up to 2 mL using Milli-Q H_2O. The initial LSRP OD of the AuNPs was maintained approximately between 0.7 ~ 1.0 for a total colloidal Au^0 range of 0.2 – 0.25 mM. All reaction solutions were acidified to pH 2 using HCl and purged with N_2 for 20 minutes. After purging, the cuvettes were sealed and stirred in the absence of light. Their UV-Vis spectra was measured to monitor the AuNP extinction at different points in time to the state of the reaction until the reaction reached equilibrium.

Etching Reactions of AuNPs by $FeCl_3$ under various CTAC concentrations

Analysis of Fe^{2+} by chemical assay

The concentration of iron(II) in a reaction mixture can be analyzed through the phenanthroline (PT) procedure.[5, 6] A standard curve was first built using standard solutions of $(NH_4)_2Fe(SO_4)^2$ at various concentrations (7.2, 14.3, 28.6, 35.8, 43.0, 64.4, and 58.9 μM). First, in a 50 mL volumetric flask half full with water, a proper amount of stock $(NH_4)_2Fe(SO_4)^2$ (0.358 mM) solution was added followed by 5 mL of sodium acetate buffer (0.735 M in 1.566 M acetic acid), 1 mL of $NH_2OH{\cdot}HCl$ (0.144 M), and 2.5 mL of PT (11.1 mM). The solution was diluted to 50 mL using water and thoroughly mixed. The absorbance at 511 nm of each standard solution was measured using a UV-Vis spectrometer in 1-cm pathlength cuvettes and plotted against its concentration to obtain the molar extinction coefficient for the $Fe(PT)_3^{2+}$ complex.

Analysis of Fe^{2+} in the equilibrated reactions was performed in a similar manner as the standards. First, 1 mL of the reaction solution was centrifuged to separate the AuNPs from the solution. The centrifugation speed and time was adjusted accordingly for each size. After separating the supernatant from the AuNP sediment, 200 uL of the supernatant was transferred into a 1-cm pathlength cuvette containing 200 uL of the acetate buffer and 100 uL of the phenanthroline solution and brought up to 2 mL with Milli-Q H_2O. The UV-Vis spectrum of the mixture was recorded and the absorbance value at 511 nm was used to calculate the iron(II) concentration through the standard curve. The calculated concentration was multiplied by 10 to get the iron(II) concentration in the equilibrium reaction mixture.

Appendix 2 – Ch. 3 Methods

Methods

Chemicals and Materials

All purchased reagents were used without any further purification unless otherwise stated. L-ascorbic acid (AA, >99%), gold (III) chloride trihydrate ($HAuCl_4 \cdot 3H_2O$, 99.995%), 1,10-phenanthroline (PT, ≥99%), and sodium borohydride ($NaBH_4$, 99.99%) were purchased form Sigma-Aldrich. Ammonium iron(II) sulfate hexahydrate ($(NH_4)_2Fe(SO_4)_2 \cdot 6H_2O$, 99%), cetyltrimethylammonium bromide (CTAB, >98.0%), cetyltrimethylammonium chloride (CTAC, >95.0%), and potassium bromide (KBr, ≥99%) were purchased from Tokyo Chemical Industry Co., LTD. Iron (III) chloride hexahydrate ($FeCl_3 \cdot 6H2O$, 99+%) and hydroxylamine hydrochloride ($NH_2OH \cdot HCl$, 99+%) were purchased from ACROS. Hydrochloric acid (HCl, 36.5%, 99.999% trace metal basis) was purchased from Alfa Aesar. Acetic acid (99.9%), and sodium acetate (≥99.7%) were purchased from Fisher Scientific. All water used for the synthesis of the AuNPs and etching reactions was purified using the Milli-Q IQ7000 system.

Instrumentation

The synthesized gold nanospheres were characterized using a JEOL JEM-2010 or FEI TALOS F200C G2 transmission electron microscope (TEM) operated at 200 kV. The reaction kinetics were monitored using UV-Vis spectrometers (Ocean Optics, Maya 2000 Pro or USB 4000). The reaction mixtures were prepared in 1-cm pathlength quartz cuvettes from Spectrocell (R-3010-T). Caps with an opening on top were used to seal the cuvettes with rubber septa. The samples were then purged using argon or nitrogen gas on Schlenk line to get rid of oxygen. Photoreactions were conducted with constant stirring at 700 rpm under irradiation using light emitting diodes (LEDs) of different wavelengths: Thorlabs M450LP1 (center wavelength: 442 nm), M470L3 (center wavelength: 462 nm), M490L4 (center wavelength: 485 nm), and M530L3(center wavelength: 517 nm). Longpass filters with a cutoff wavelength at 446 nm (Thorlabs FELH0450) were inserted in front of the 442 nm, 462 nm, and 485 nm LEDs, whereas longpass filters with a cutoff wavelength at 495 nm (Thorlabs FGL495) were used for the 517 nm LEDs. This is to prevent or reduce photoinduced reduction of iron(III) chloride by blue light.[7] The spectra of the LED and longpass filter combinations are presented in Figure 15. The center wavelength of the LED and longpass filter combinations are 450 nm, 462 nm, 490 nm, and 517 nm respectively. The LED light was focused to a spot size of less than 1 cm x 1 cm to ensure that all the light passes through the cuvette during photoreaction. The optical power was measured using Thorlabs power meters (PM100D with a S170C photo sensor).

Synthesis of Gold Nanospheres

The gold nanospheres used in this study were prepared following the same procedures as reported by Zheng et al.,[3] except that the volumes of reagents used for the synthesis of 10 nm to 35 nm particles were scaled up by 100 times so that more particles can be prepared

through each synthesis. The final synthesized particles were collected by centrifugation and washed with 100 mM CTAC for three times. The product gold nanospheres were stored in 100 mM CTAC for later use.

Etching Reactions of Gold Nanospheres Using Iron(III) under Dark and Photo-Irradiation Conditions

In a 1-cm pathlength cuvette, solutions of $FeCl_3$ (4 mM, 125 µL), gold nanospheres (in 20 mM CTAC, 150 µL), and CTAB (2 mM, 1.1 mL, pH 1.75) were diluted to 2 mL using water. The absorbance of the gold nanospheres at the surface plasmon resonance band is controlled at 0.83 OD at the beginning of the reaction by adjusting the gold nanosphere concentration in the 20 mM CTAC solution. With stirring, the reaction mixture was purged using argon or nitrogen gas for 20 minutes and sealed tightly. Before beginning the reaction, each sample's UV-Vis absorption spectrum was recorded. The reactions were allowed to proceed with stirring (700 rpm) under dark or constant light illumination using LEDs of different wavelengths (450, 462, 490, and 517 nm). Their spectra were recorded at different time intervals until the reactions reached equilibria.

Reverse Reaction of Gold Nanospheres Using Iron(II) under Dark and Photo-Excitation

These reactions were performed similarly to the iron(III) etching reactions mentioned above with some changes to the reaction mixtures. In a 1-cm pathlength cuvette, $FeCl_2$ (6.236 mM, 64 µL), 11.3 nm diameter gold nanospheres (in H_2O, 200 µL), freshly prepared $AuCl_2^-$ (1.67 mM in 20 mM CTAC, 240 µL), and CTAB (2 mM pH 1.75, 1100 µL) were diluted to 2 mL using water. The absorbance at LSPR at the start of each reaction was ca. 0.026 OD. The samples were purged using high-purity nitrogen gas for 20 minutes under constant stirring. The reactions were allowed to react under similar conditions as mentioned previously.

Preparation of $AuCl_2^-$ in 20 mM CTAC solution

Due to the lack of commercially available halide gold(I) precursors, $AuCl_2^-$ was prepared by photo-reduction of solutions of $HAuCl_4$ in the presence of CTAC. Briefly, in a loosely-capped cuvette, $HAuCl_4$ (25 mM, 133.6 µL) and CTAC (100 mM, 400 µL) were diluted to 2 mL and illuminated using a 375 nm LED for 15 minutes. The solution turns from cloudy yellow to colorless, which indicates the reduction of Au(III) to Au(I). The reduction is complete when the UV-Vis absorbance peak at 330 nm is no longer detected.[8] Prior to each use, the $AuCl_2^-$ solution was warmed in a 60 °C water bath for 30 seconds to re-dissolve the $AuCl_2^-$ precipitates.

Qualitative test of gold(I) and gold(III) in equilibrium reaction mixtures

For the qualitative test of gold(III), after a reaction has reached equilibrium, 200 uL of the reaction mixture was transferred to a 2-mm pathlength cuvette and a spectrum was recorded immediately. This is followed by the addition of 10 uL of concentrated phosphoric acid (85%) to "shield" the yellow color of $FeBr_3$ and $FeCl_3$ because phosphoric acid can form a colorless complex with Fe^{3+}.[9, 10] Then, 200 uL of CTAB (100 mM) was added to the 200

uL reaction mixture in the cuvette and a second spectrum was recorded. Judging by the presence or absence of the gold(III)-CTAB complex absorption peak at ~ 390 nm, the presence or absence of gold(III) in the equilibrium reaction mixture can be tested. In all the reactions, gold(III) was not detected.

As for the qualitative test of gold(I), the same procedure described above was used with two modifications. Firstly, the reaction mixture was centrifuged at high speed (14,500 rpm) for 15 min to remove all the AuNPs in the reaction mixture. Secondly, after the addition of CTAB (the solution remains colorless at this step), 100 uL of 30% hydrogen peroxide was added. The solution immediately turned yellow with the appearance of an absorption peak at 390 nm, which is due to the oxidation of Au(I) to Au(III) by hydrogen peroxide. The Au(III) and Au(I) tests proved that the etching product at equilibrium was Au(I) instead of Au(III), which is consistent with previous reports.[9, 11, 12] Example spectra for these test can be found in Figure 16.

Quantitative analysis of iron(II) in equilibrium reaction mixtures

The concentration of iron(II) in a reaction mixture can be analyzed through the phenanthroline (PT) procedure.[5, 13] A standard curve was first built using standard solutions of $(NH_4)_2Fe(SO_4)_2$at various concentrations (7.2, 14.3, 28.6, 35.8, 43.0, 64.4, and 58.9 μM). First, in a 50 mL volumetric flask half full with water, a proper amount of stock $(NH_4)_2Fe(SO_4)_2$ (0.358 mM) solution was added followed by 5 mL of sodium acetate buffer (0.735 M in 1.566 M acetic acid), 1 mL of $NH_2OH{\cdot}HCl$ (0.144 M), and 2.5 mL of PT (11.1 mM). The solution was diluted to 50 mL using water and thoroughly mixed. The absorbance at 511 nm of each standard solution was measured using a UV-Vis spectrometer in 1-cm pathlength cuvettes and plotted against its concentration to obtain the molar extinction coefficient for the $Fe(PT)_3^{2+}$ complex.

After each reaction reaches equilibrium, 1 mL of the reaction mixture was centrifuged at 14,500 rpm for 15 min to remove all AuNPs. Then 200 uL of the supernatant was mixed in a 1-cm pathlength cuvette with 200 uL of the acetate buffer and 100 uL of the phenanthroline solution. Water was then added to bring the total volume to 2 mL. The UV-Vis spectrum of the mixture was taken and the absorbance value at 511 nm was used to calculate the iron(II) concentration through the standard curve. The calculated concentration was multiplied by 10 to get the iron(II) concentration in the equilibrium reaction mixture.

Calculations of iron(III) and gold(I) concentrations in equilibrium reaction mixtures

The concentration of iron(III) in the equilibrium reaction mixtures can be calculated by subtracting the iron(II) concentration at reaction equilibrium from the total iron(III) concentration that was in the reaction mixture in the beginning. The iron(III) concentration in the stock solution was confirmed to be accurate using a previously reported photochemical phenanthroline method.[6, 13, 14] Since there was no gold(III) complex detected at reaction equilibrium (see Figure 16), the reaction products were gold(I) and

iron(II). The concentration of gold(I) can be calculated using the amount of gold etched, which can be easily calculated using the absorbance change of the plasmon resonance peak because the molar absorption coefficient of gold nanospheres is proportional to the third power of the diameter.[15, 16] Considering that the stability constant of $AuBr_2^-$ complex is very high (~10^{12})[17] and the amount of bromide ions in the reaction mixture is several times higher than that of the total amount of gold (>4 times), we assume that all the gold(I) ions exist in the $AuBr_2^-$ complex to simplify the calculations. Therefore, the $AuBr_2^-$ concentration is estimated as the same as the amount of gold etched. The free bromide ion concentration is estimated as the total bromide ion concentration subtracted by two times the concentration of $AuBr_2^-$.

Calculation of redox potential $\left[E^0_{AuBr_2^-/Au}\right]^{NP_n}$

As for the calculation of $\left[E^0_{AuBr_2^-/Au}\right]^{NP_n}$, we combine equations (1) and (2) in the main text to get:

$$AuNP_n + Fe^{3+} + 2Br^- \leftrightharpoons AuNP_{n-1} + Fe^{2+} + AuBr_2^- \quad \text{(S1)}$$

At equilibrium, the cell potential will be zero:

$$E_{cell} = E^0_{Fe^{3+}/Fe^{2+}} - \left[E^0_{AuBr_2^-/Au}\right]^{NP_n} - \frac{RT}{F} ln \frac{[AuBr_2^-][Fe^{2+}]}{[Br^-]^2[Fe^{3+}]} = 0 \quad \text{(S2)}$$

Therefore,

$$\left[E^0_{AuBr_2^-/Au}\right]^{NP_n} = E^0_{Fe^{3+}/Fe^{2+}} - \frac{RT}{F} ln \frac{[AuBr_2^-]\left[Fe^{2+}\right]}{[Br^-]^2\left[Fe^{3+}\right]} \quad \text{(S3)}$$

Calculation of the half-cell potential

The cathode ($Fe^{3+} + e^- \rightarrow Fe^{2+}$) half-cell potential and the anode half-cell potential ($Au^+ + e^- \rightarrow Au$) of the reaction should be equal at equilibrium. So, we only need to calculate the cathode half-cell potential:

$$E_{reduction} = E^0_{Fe^{3+}/Fe^{2+}} - \frac{RT}{F} ln \frac{[Fe^{2+}]}{[Fe^{3+}]} \quad \text{(S4)}$$

Example calculation of the redox potential

To demonstrate how to calculate the redox potentials, we choose to use as an example one of the data sets for the photoinduced oxidative etching of 34.9 nm AuNPs under 490 nm light irradiation at 100 mW incident power. The initial plasmon absorbance of the sample was 0.82 OD, whereas that of the sample at the equilibrium was 0.41 OD. Since the molar absorption coefficient of gold nanospheres at the surface plasmon peak is roughly proportional to third power of the radius,[16] we can estimate the number of etched gold atoms based on the decrease of the plasmon absorbance. Details of this calculation has been reported in a previous paper published by this group.[15] This number is equal to the number

of gold(I) ions formed during the etching reaction because there was no gold(III) present in the equilibrium solution mixture. Since the solubility constant of $AuBr_2^-$ is three orders of magnitude higher than that of $AuCl_2^-$, all gold(I) ions are assumed to exist in the form of $AuBr_2^-$. Therefore, the $AuBr_2^-$ concentration can be estimated to be 1.05×10^{-4} M. The concentration of bromide ions in the beginning of the reaction (from CTAB) is 1.10×10^{-3} M. Therefore, the concentration of free bromide ions at the equilibrium is 1.10×10^{-3} M – 1.05×10^{-4} M $\times 2 = 8.90 \times 10^{-4}$ M. The total iron(III) concentration at the beginning of the etching reaction is 2.52×10^{-4} M. The concentration of iron(II) at the equilibrium was determined to be 9.06×10^{-5} M through the phenanthroline assay. So the concentration of iron(III) at the equilibrium is 2.52×10^{-4} M - 9.06×10^{-5} M = 1.62×10^{-4} M. The stability constant of $AuBr_2^-$ is 1×10^{12} M^{-2}.[17] The standard redox potential $E^0_{Fe^{3+}/Fe^{2+}}$ is 0.77 V.[9] The ideal gas constant R = 8.314 J · mol^{-1} · K^{-1}, the temperature T is 298 K, and the Faraday's constant F = 96485.33 C mol^{-1}.

The redox potential $\left[E^0_{Au^+/Au}\right]^{NP_n}$ can be calculated using equation (6) in the main text:

$$\left[E^0_{Au^+/Au}\right]^{NP_n} = E^0_{Fe^{3+}/Fe^{2+}} - \frac{RT}{F} ln \frac{[AuBr_2^-][Fe^{2+}]}{\beta[Br^-]^2[Fe^{3+}]} = 1.37\ V$$

The redox potential $\left[E^0_{AuBr_2^-/Au}\right]^{NP_n}$ can be calculated using equation (S3) in the supporting information:

$$\left[E^0_{AuBr_2^-/Au}\right]^{NP_n} = E^0_{Fe^{3+}/Fe^{2+}} - \frac{RT}{F} ln \frac{[AuBr_2^-][Fe^{2+}]}{[Br^-]^2[Fe^{3+}]} = 0.66\ V$$

The half-cell potential can be calculated using equation (S4) in the supporting information:

$$E_{reduction} = E^0_{Fe^{3+}/Fe^{2+}} - \frac{RT}{F} ln \frac{[Fe^{2+}]}{[Fe^{3+}]} = 0.79\ V$$

Estimation of the influence of gold nanosphere size on the redox potential

The difference between the redox potential of small metallic nanospheres from the bulk value can be estimated according to the following equation,[18, 19]

$$\left[E^0_{M^+/M}\right]^{NP_n} = \left[E^0_{M^+/M}\right]^{bulk} - \frac{2\gamma V_m}{F}\left(\frac{1}{r}\right)$$

(S5)

where γ is the surface tension, V_m is the molar volume, r is the radius of the nanosphere, F is the Faraday constant, n is the number of metal atoms in each NP (NP).

Basically, smaller particles have lower redox potential. To estimate the effect of particle size on the redox potential in our etching experiment, we need to estimate the reduction of redox potential when we assume the AuNP size changes from its equilibrium value under the dark condition (r_d) to that under photoirradiation condition of wavelength λ (r_λ):

$$\left[\Delta E^0_{M^+/M}\right]^{NP}_{Size} = \left(-\frac{2\Upsilon V_m}{F}\right)\left(\frac{1}{r_\lambda}\right) - \left(-\frac{2\Upsilon V_m}{F}\right)\left(\frac{1}{r_d}\right) = \left(\frac{2\Upsilon V_m}{F}\right)\left(\frac{1}{r_d} - \frac{1}{r_\lambda}\right) \quad \text{(S6)}$$

For gold, the surface tension at 25 °C is 1.88 J m^{-2}, V_m is 10.21 cm^3 mol^{-1}, F = 96485.33 C mol^{-1}. The average diameters (D = 2r) of the gold nanospheres under dark and photoirradiation conditions of different wavelengths are listed in Table 1. The calculated change of redox potential due to size effect are presented as well. As we can see, the calculated size effect is much smaller than the experimental value. Thus, the size effect is not the main contributing factor to the wavelength-dependent change of redox potential.

It is important to note that equation (S5) does not include the effect of the charge of the metallic NPs. According to Lee et al.,[20] the redox potential with the combination of charge effect and size effect taken into account is

$$\left[E^0_{M^+/M}\right]^{NP_n} = \left[E^0_{M^+/M}\right]^{bulk} - \frac{2\Upsilon V_m}{F}\left(\frac{1}{r}\right) + \frac{V_m}{8\pi F r^4}\frac{z^2e^2}{4\pi\varepsilon_0\varepsilon_r} \quad \text{(S7)}$$

where z is the number of charges on each NP, $\varepsilon_0 = 8.85 \times 10^{-12}\ F/m$ is the vacuum permittivity, ε_r is the relative permittivity of the surrounding medium (in this case, it is water: $\varepsilon_r = 80.2$ at room temperature). The sign of the last term will be positive if z is positive and negative if z is negative. In this study, the sign should be negative because the NPs are photocharged with electrons.

The number of accumulated charges on the AuNPs in this study cannot be determined directly from the concentrations of hole quencher and electron acceptor because the experimental errors of iron(II) and gold(I) concentrations are larger than their discrepancy. According to other studies, the number of electrons or holes that can be accumulated on a metallic NP or semiconductor NP with a size around 10 to 15 nm has been reported to be in the range of 10 to 500.[19, 21-26] Using these reference numbers, we can evaluate the influence of the size of charged AuNPs to the redox potential in our study by assuming each particle has an average number of charges within a range of 10 to 500 electrons. Using equation (S7), we can estimate the size effect on the redox potential with charges on each NP taken into account in our etching experiment. The reduction of redox potential, when we assume the AuNP size changes from its equilibrium value under the dark condition (r_d) to that under photoirradiation condition of wavelength λ (r_λ), can be calculated as (assuming the number of electrons accumulated on each particle is the same):

$$\left[\Delta E^0_{M^+/M}\right]^{NP}_{Size\ and\ Charge} = \left[\left(-\frac{2\Upsilon V_m}{F}\right)\left(\frac{1}{r_\lambda}\right) - \frac{V_m}{8\pi F r_\lambda{}^4}\frac{z^2e^2}{4\pi\varepsilon_0\varepsilon_r}\right] - \left[\left(-\frac{2\Upsilon V_m}{F}\right)\left(\frac{1}{r_d}\right) - \frac{V_m}{8\pi F r_d{}^4}\frac{z^2e^2}{4\pi\varepsilon_0\varepsilon_r}\right] = \left(\frac{2\Upsilon V_m}{F}\right)\left(\frac{1}{r_d} - \frac{1}{r_\lambda}\right) - \frac{V_m}{8\pi F}\frac{z^2e^2}{4\pi\varepsilon_0\varepsilon_r}\left(\frac{1}{r_\lambda{}^4} - \frac{1}{r_d{}^4}\right) \quad \text{(S8)}$$

The results of this estimation are listed in Table 1 which show that the size effect to the redox potential does not differ much no matter whether the particles were charged or not.

Tables

Table 1. Comparison of the size and charge effects (equation S6) on the redox potential to that of photoirradiation at different wavelengths. Reprinted with permission from Ref.[27] Copyright 2020 American Chemical Society.

Wavelength (nm)	**Dark**	**517**	**490**	**462**	**450**
Incident Power (mW)	NA	100	100	111	111
Average equilibrium diameter (nm)	32.0	27.7	23.9	12.5	12.9
$\left[\Delta E^{0}_{Au^{+}/Au}\right]^{NP}_{Size}$ **(mV)**	NA	3.81	8.37	38.6	36.6
$\left[\Delta E^{0}_{Au^{+}/Au}\right]^{NP}_{Size\ and\ 10\ e^{-}}$ **(m V)**	NA	3.81	8.37	38.6	36.6
$\left[\Delta E^{0}_{Au^{+}/Au}\right]^{NP}_{Size\ and\ 500\ e^{-}}$ **(mV)**	NA	3.85	8.47	40.5	38.2
$\left[\Delta E^{0}_{Au^{+}/Au}\right]^{NP}_{Nernst}$ **(mV)**	NA	77.0	114	177	200

Notes:

1. $\left[\Delta E^{0}_{Au^{+}/Au}\right]^{NP}_{Size}$ *is the calculated reduction of redox potential due to the decrease in the equilibrium gold nanosphere sizes under photoirradiation of a certain wavelength versus the dark condition.*
2. $\left[\Delta E^{0}_{Au^{+}/Au}\right]^{NP}_{Size\ and\ 10\ e^{-}}$ *is the calculated reduction of redox potential due to the decrease in the equilibrium gold nanosphere sizes under photoirradiation of a certain wavelength versus the dark condition, assuming that each particle has 10 electrons.*
3. $\left[\Delta E^{0}_{Au^{+}/Au}\right]^{NP}_{Size\ and\ 500\ e^{-}}$ *is the calculated reduction of redox potential due to the decrease in the equilibrium gold nanosphere sizes under photoirradiation of a certain wavelength versus the dark condition, assuming that each particle has 500 electrons.*
4. $\left[\Delta E^{0}_{Au^{+}/Au}\right]^{NP}_{Nernst}$ *is the reduction of the redox potential under photoirradiation of a certain wavelength compared to that of the dark condition, calculated using the Nernst equation based on experimental data.*

5. *Three batches of NP samples with average sizes of 30.9. 32.8, and 34.9 nm were used for the etching reactions.*

Table 2. Calculated redox potential $\left[E^0_{Au^+/Au}\right]^{NP_n}$ (using equation 6 in the main text), $\left[E^0_{AuBr_2^-/Au}\right]^{NP_n}$ (using equation S3), incident power, absorbed power, and average diameter of NPs at equilibria as a function of irradiation wavelength for the photooxidative etching reaction. Reprinted with permission from Ref.[27] Copyright 2020 American Chemical Society.

Wavelength (nm)	$\left[E^0_{Au^+/Au}\right]^{NP_n}$ **(V vs SHE)**	$\left[E^0_{AuBr_2^-/Au}\right]^{NP_n}$ **(V vs SHE)**	**Incident Power (mW)**	**Absorbed Power (mW)**	**D_eq (nm)**
450	1.280 ± 0.004	0.570 ± 0.004	111	6.25	12.9
462	1.30 ± 0.01	0.59 ± 0.01	111	9.74	12.5
490	1.37 ± 0.01	0.66 ± 0.01	100	43.8	23.9
517	1.403 ± 0.008	0.693 ± 0.008	100	67.5	27.7
Dark	1.480 ± 0.004	0.770 ± 0.004	NA	NA	32.0

Notes: The etching reactions were conducted for three batches of NPs with average diameters of 30.9 nm, 32.8 nm, and 34.9 nm. D_eq is the average diameter of the NPs at equilibria. Absorbed power is the average absorbed power by the reaction mixture at equilibria.

Table 3. Calculated redox potential $\left[E^0_{Au^+/Au}\right]^{NP_n}$ (using equation 6 in the main text), incident power, absorbed power, and average diameter of NPs at equilibria as a function of irradiation wavelength for the etching of nanospheres with an initial size of 11.3 nm. Reprinted with permission from Ref.[27] Copyright 2020 American Chemical Society.

Wavelength (nm)	$\left[E^0_{Au^+/Au}\right]^{NP_n}$ **(V vs SHE)**	**Incident Power (mW)**	**Absorbed Power (mW)**	**D_eq (nm)**
450	1.2922 ± 0.0001	111	9.40	3.70
462	1.302 ± 0.003	117	13.9	3.79
490	1.4010 ± 0.0003	110	68.1	10.2
517	1.430 ± 0.002	95.8	72.5	10.8
Dark	1.455 ± 0.002	NA	NA	10.9

Notes: D_eq is the average diameter of the NPs at equilibria. Absorbed power is the average absorbed power by the reaction mixture at equilibria.

Table 4. Calculated redox potential (using equation 6 in the main text) presented as a function of optical power Reprinted with permission from Ref.[27] Copyright 2020 American Chemical Society.

Wavelength (nm)	**Incident Power (mW)**	**Absorbed Power (mW)**	**D_eq (nm)**	$\left[E^{0}_{Au^{+}/Au}\right]^{NP_n}$ **(V vs SHE)**
450	11.0	0.38	6.81	1.334 ± 0.006
	55.1	5.69	10.9	1.290 ± 0.008
	111	6.25	12.9	1.280 ± 0.004
462	18.7	1.28	8.36	1.316 ± 0.001
	111	9.74	12.5	1.30 ± 0.01
	191	21.9	13.8	1.298 ± 0.003
490	10.3	7.01	29.1	1.451 ± 0.005
	46.2	28.2	29.1	1.437 ± 0.001
	101	43.8	23.9	1.37 ± 0.01
517	16.0	11.2	27.2	1.440 ± 0.007
	100	67.5	27.7	1.403 ± 0.008
	164	107	31.1	1.406 ± 0.008

Notes: D_eq is the average diameter of the NPs at equilibria. Absorbed power is the average absorbed power by the reaction mixture at equilibria. The etching reactions were conducted for three batches of NPs with average diameters of 30.9 nm, 32.8 nm, and 34.9 nm.

Figures

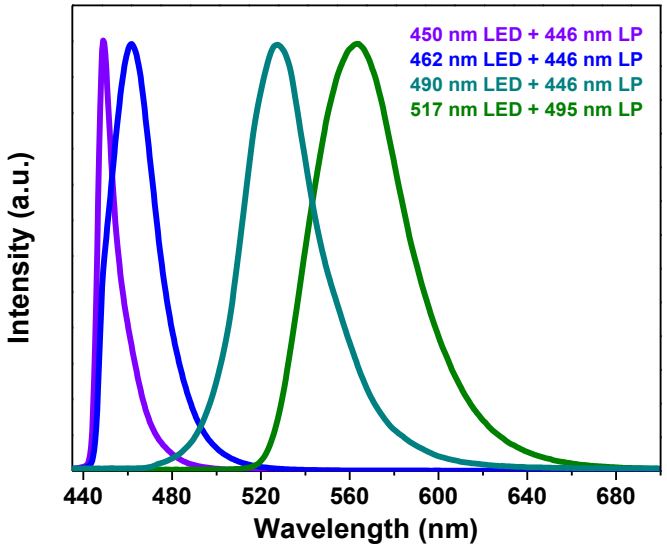

Figure 15. Spectra of the LEDs (along with longpass filters) used in this study. The peaks of the spectra are at 450 nm (purple), 462 nm (blue), 490 nm (cyan), and 517 nm (olive) respectively. LP stands for longpass filter. Reprinted with permission from Ref.[27] Copyright 2020 American Chemical Society.

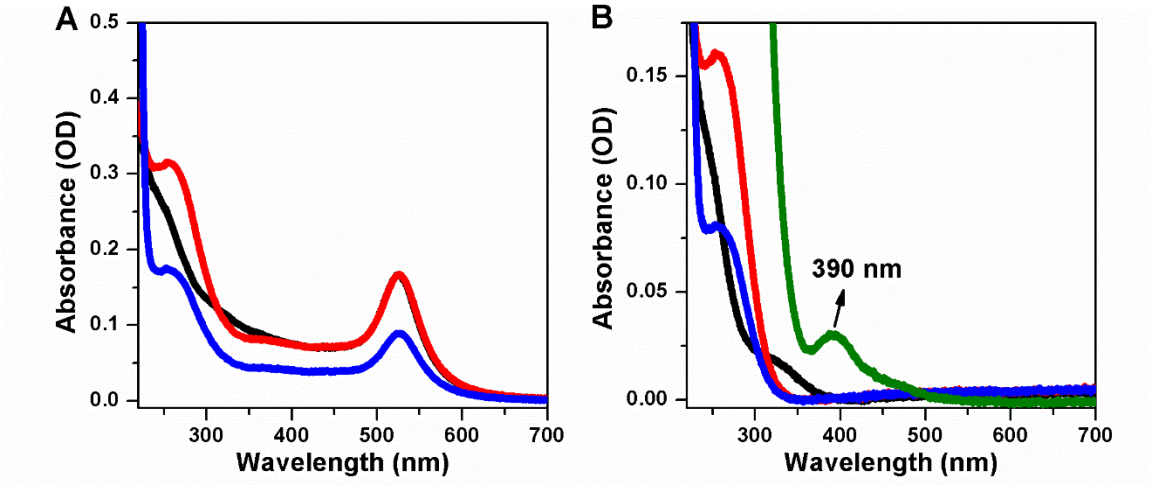

Figure 16. UV-Vis spectra showing the absence of gold(III) ions (A) and presence of gold(I) ions (B) in the equilibrium reaction mixture. The tests were done using the equilibrium reaction mixture without (A) and with (B) gold nanospheres removed through centrifugation. The black lines represent the spectra of the reaction mixture, the red lines represent the spectra when phosphoric acid was added into the reaction mixture, the blue lines represent the spectra when both phosphoric acid and CTAB were added, and the olive line in (B) represents the spectrum of the supernatant when phosphoric acid, CTAB and hydrogen peroxide were added successively. Details of these experiments can

be found on page 3 of the supporting information. Reprinted with permission from Ref.[27] Copyright 2020 American Chemical Society.

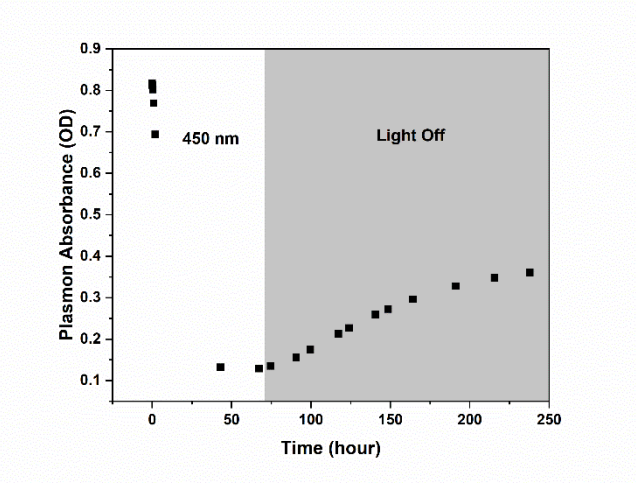

Figure 17. Reaction kinetics of the photooxidative etching and regrowth of the 30.9 nm AuNPs monitored at the LSPR peak. The reaction mixture was irradiated by a 450 nm LED at 110 mW incident power for 70 hours, during which the reaction reached equilibrium. Then, the light was turned off after which the particles started to regrow slowly (gray shaded area). Reprinted with permission from Ref.[27] Copyright 2020 American Chemical Society.

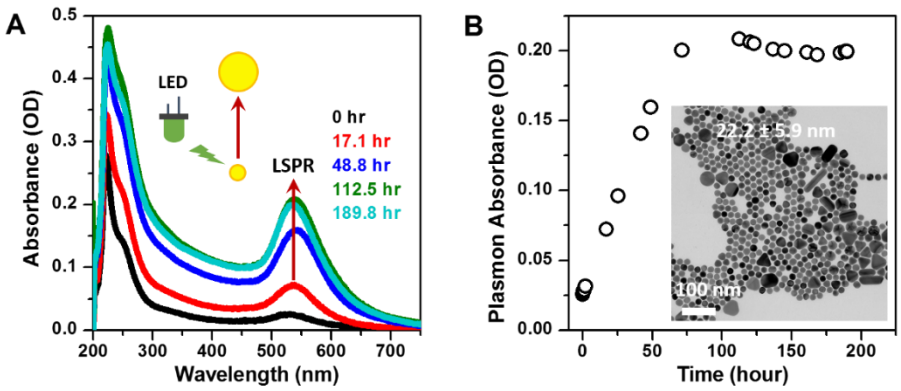

Figure 18. Time-dependent spectral change (A) and kinetics (B, monitored at the LSPR peak of the gold nanospheres) of the reverse reaction starting with 11.3 nm gold nanospheres under 450 nm irradiation at 100 mW. The inset in panel B shows the TEM image of the NPs at the equilibrium of the reverse reaction. Reprinted with permission from Ref.[27] Copyright 2020 American Chemical Society.

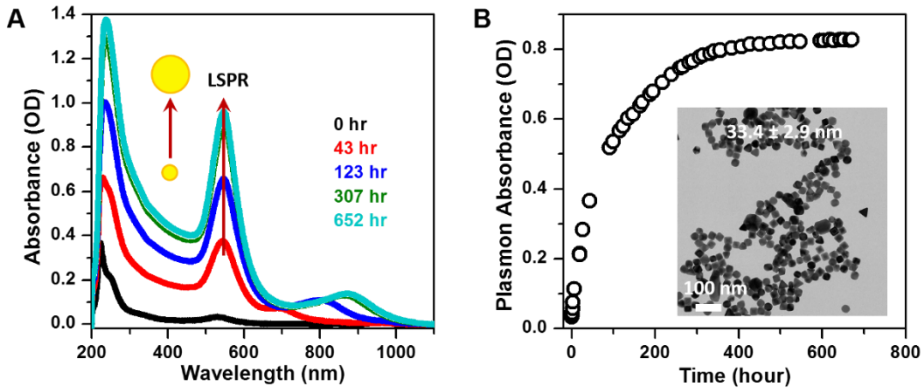

Figure 19. Time-dependent spectral change (A) and kinetics (B, monitored at the LSPR peak of the gold nanospheres) of the reverse reaction starting with 11.3 nm gold nanospheres under dark. The inset in panel B shows the TEM image of the NPs at the equilibrium of the reverse reaction. Reprinted with permission from Ref.[27] Copyright 2020 American Chemical Society.

It can be seen from Figure S4 and S5 that although most of the particles at the reverse reaction equilibria are spherical and have similar size, some particles are smaller or larger, or have grown into irregular shapes. A shoulder at long wavelength also appeared in the UV-Vis spectra of the reverse reaction solution under dark, which indicates the possible presence of AuNPs of non-spherical shapes (e.g. nanocubes, nanorods, or octahedrons).

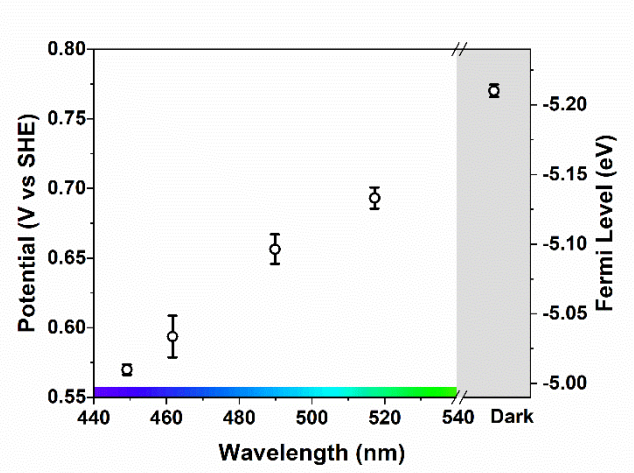

Figure 20. The dependence of the redox potential $\left[E^0_{AuBr_2^-/Au}\right]^{NP_n}$ of gold nanospheres on the wavelength of photoirradiation at incident power of about 100 mW (etching gold nanospheres with average sizes of 30.8, 32.8, and 34.9 nm), compared with dark condition (shaded area). The right vertical axis shows the Fermi level (E_{Fermi}) corresponding to the redox potential relative to the vacuum level: $E_{Fermi}(\text{eV}) = -4.44\ \text{eV} - e \cdot E_{redox}(\text{V vs SHE})$.[28] Experimental uncertainty is reported as one standard error. Reprinted with permission from Ref.[27] Copyright 2020 American Chemical Society.

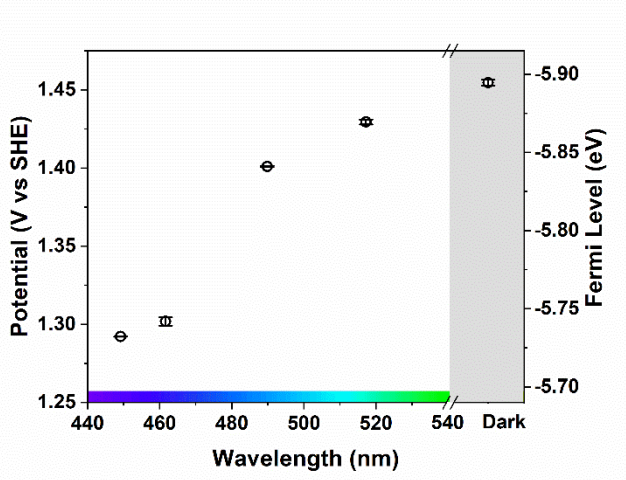

Figure 21. The dependence of the redox potential $\left[E^0_{Au^+/Au}\right]^{NP_n}$ of gold nanospheres on the wavelength of photoirradiation at incident power of about 100 mW (etching 11.3 nm gold nanospheres), compared with dark condition (shaded area). The right vertical axis shows the Fermi level (E_{Fermi}) corresponding to the redox potential relative to the vacuum level: $E_{Fermi}(\text{eV}) = -4.44\ \text{eV} - e \cdot E_{redox}(\text{V vs SHE})$.[28] Experimental uncertainty is reported as one standard error. Reprinted with permission from Ref.[27] Copyright 2020 American Chemical Society.

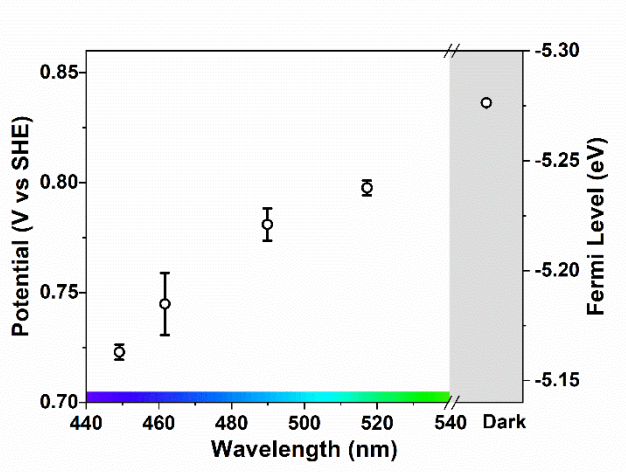

Figure 22. The dependence of the reduction half-cell potential of the reaction mixture on the wavelength of photoirradiation at the incident power of about 100 mW (etching gold nanospheres with average sizes of 30.8, 32.8, and 34.9 nm), compared with dark condition (shaded area). The right vertical axis shows the Fermi level (E_{Fermi}) corresponding to the redox potential relative to the vacuum level: $E_{Fermi}(\text{eV}) = -4.44\ \text{eV} - e \cdot E_{reduction}(\text{V vs SHE})$.[28] Experimental uncertainty is reported as one standard error. Reprinted with permission from Ref.[27] Copyright 2020 American Chemical Society.

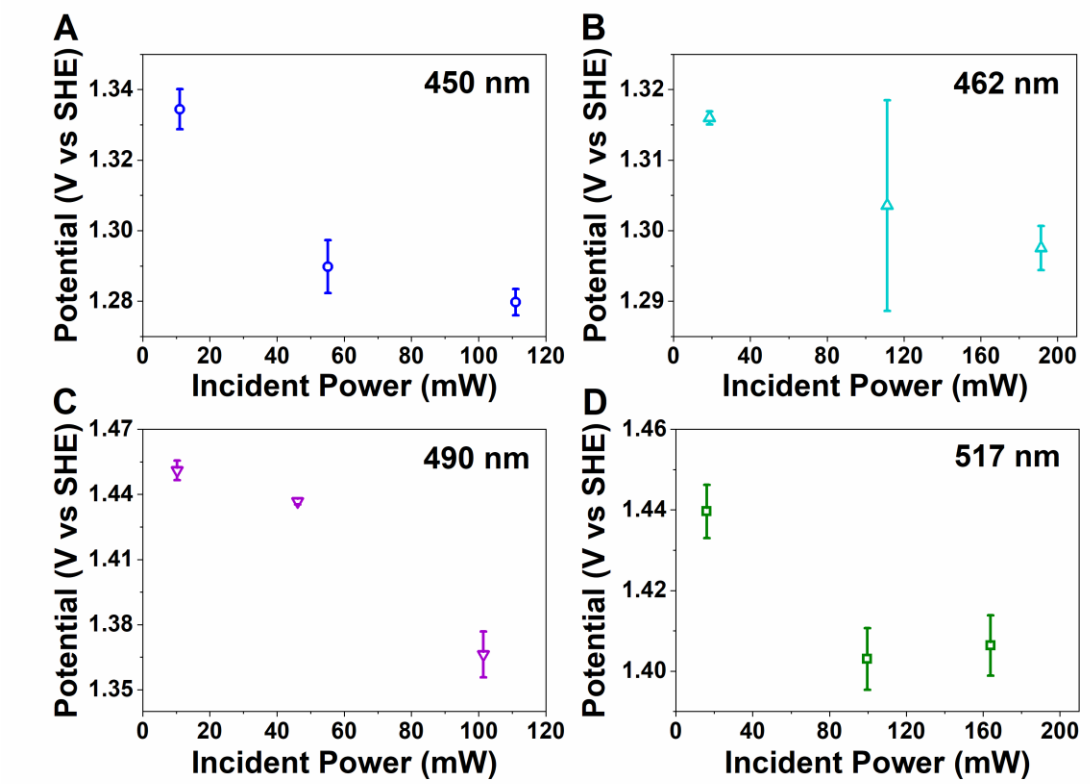

Figure 23. The dependence of redox potential $E^0_{Au^+/Au^*}$ of AuNPs (etching 30 nm gold nanospheres) on incident optical power under light irradiation of 450 nm (A, blue), 462 nm (B, cyan), 490 nm (C, purple), and 517 nm (D, olive). Experimental uncertainty is reported as one standard error. Reprinted with permission from Ref.[27] Copyright 2020 American Chemical Society.

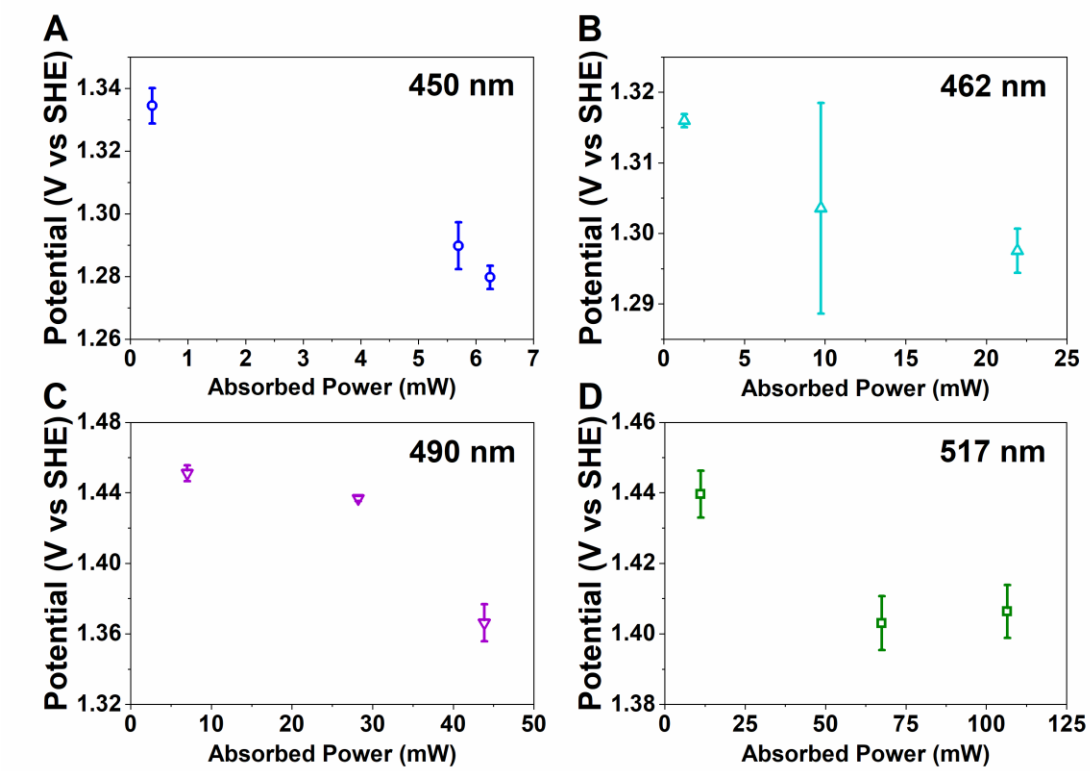

Figure 24. The dependence of redox potential $E^0_{Au^+/Au^*}$ of AuNPs (etching 30 nm gold nanospheres) on absorbed optical power under light irradiation of 450 nm (A, blue), 462 nm (B, cyan), 490 nm (C, purple), and 517 nm (D, olive). The absorbed power is the power absorbed by the sample at equilibrium at the excitation wavelength. Experimental uncertainty is reported as one standard error. Reprinted with permission from Ref.[27] Copyright 2020 American Chemical Society.

Appendix 2 References

(1) Bratlie, K. M.; Lee, H.; Komvopoulos, K.; Yang, P.; Somorjai, G. A. Platinum Nanoparticle Shape Effects on Benzene Hydrogenation Selectivity. *Nano Lett.* **2007**, *7* (10), 3097-3101. DOI: 10.1021/nl0716000.

(2) Chiu, C.-Y.; Chung, P.-J.; Lao, K.-U.; Liao, C.-W.; Huang, M. H. Facet-Dependent Catalytic Activity of Gold Nanocubes, Octahedra, and Rhombic Dodecahedra toward 4-Nitroaniline Reduction. *The Journal of Physical Chemistry C* **2012**, *116* (44), 23757-23763. DOI: 10.1021/jp307768h.

(3) Zheng, Y. Q.; Zhong, X. L.; Li, Z. Y.; Xia, Y. N. Successive, Seed-Mediated Growth for the Synthesis of Single-Crystal Gold Nanospheres with Uniform Diameters Controlled in the Range of 5-150 nm. *Particle & Particle Systems Characterization* **2014**, *31* (2), 266-273. DOI: 10.1002/ppsc.201300256.

(4) Yoon, S.; Kim, C.; Lee, B.; Lee, J. H. From a precursor to an etchant: spontaneous inversion of the role of Au(iii) chloride for one-pot synthesis of smooth and spherical gold nanoparticles. *Nanoscale Advances* **2019**, 10.1039/C9NA00157C. DOI: 10.1039/C9NA00157C.

(5) Saywell, L. G.; Cunningham, B. B. Determination of Iron: Colorimetric o-Phenanthroline Method. *Industrial & Engineering Chemistry Analytical Edition* **1937**, *9* (2), 67-69. DOI: 10.1021/ac50106a005.

(6) Stucki, J. W. The Quantitative Assay of Minerals for Fe2+ and Fe3+ Using 1,10-Phenanthroline .2. A Photochemical Method. *Soil Sci Soc Am J* **1981**, *45* (3), 638-641. DOI: DOI 10.2136/sssaj1981.03615995004500030040x.

(7) Plieth, W. J. Electrochemical Properties of Small Clusters of Metal Atoms and Their Role in Surface Enhanced Raman-Scattering. *J. Phys. Chem.* **1982**, *86* (16), 3166-3170. DOI: DOI 10.1021/j100213a020.

(8) Sivan, Y.; Baraban, J.; Un, I. W.; Dubi, Y. Comment on "Quantifying Hot Carrier and Thermal Contributions in Plasmonic Photocatalysis". *Science* **2019**, *364* (6439). DOI: ARTN eaaw9367

10.1126/science.aaw9367.

(9) Zou, R.; Guo, X.; Yang, J.; Li, D.; Peng, F.; Zhang, L.; Wang, H.; Yu, H. Selective etching of gold nanorods by ferric chloride at room temperature. *CrystEngComm* **2009**, *11* (12), 2797-2803, 10.1039/B911902G. DOI: 10.1039/B911902G.

(10) Cai, S.; HUang, C. *Noble Metal Analysis*; Metallurgical Industry Press, 1984.

(11) Tsung, C. K.; Kou, X. S.; Shi, Q. H.; Zhang, J. P.; Yeung, M. H.; Wang, J. F.; Stucky, G. D. Selective shortening of single-crystalline gold nanorods by mild oxidation. *Journal of the American Chemical Society* **2006**, *128* (16), 5352-5353. DOI: 10.1021/ja060447t.

(12) Sreeprasad, T. S.; Samal, A. K.; Pradeep, T. Body- or tip-controlled reactivity of gold nanorods and their conversion to particles through other anisotropic structures. *Langmuir* **2007**, *23* (18), 9463-9471. DOI: 10.1021/la700851x.

(13) Stucki, J. W.; Anderson, W. L. The Quantitative Assay of Minerals for Fe2+ and Fe3+ Using 1,10-Phenanthroline .1. Sources of Variability. *Soil Sci Soc Am J* **1981**, *45* (3), 633-637. DOI: DOI 10.2136/sssaj1981.03615995004500030039x.

(14) Komadel, P.; Stucki, J. W. Quantitative Assay of Minerals for Fe-2+ and Fe-3+ Using 1,10-Phenanthroline .3. A Rapid Photochemical Method. *Clay Clay Miner* **1988**, *36* (4), 379-381. DOI: Doi 10.1346/Ccmn.1988.0360415.
(15) Mao, Z.; Vang, H.; Garcia, A.; Tohti, A.; Stokes, B. J.; Nguyen, S. C. Carrier Diffusion—The Main Contribution to Size-Dependent Photocatalytic Activity of Colloidal Gold Nanoparticles. *ACS Catal.* **2019**, *9* (5), 4211-4217. DOI: 10.1021/acscatal.9b00390.
(16) Near, R. D.; Hayden, S. C.; Hunter, R. E.; Thackston, D.; El-Sayed, M. A. Rapid and Efficient Prediction of Optical Extinction Coefficients for Gold Nanospheres and Gold Nanorods. *The Journal of Physical Chemistry C* **2013**, *117* (45), 23950-23955. DOI: 10.1021/jp4082596.
(17) Nicol, M. J.; Fleming, C. A.; Paul, R. L. The chemistry of the extraction of gold. In *The Extractive Metallurgy of Gold in South Africa*, Stanley, G. G. Ed.; Vol. Chapter 15; South African Institute of Mining and Metallurgy, 1987; pp 831-906.
(18) Plieth, W. J. Electrochemical properties of small clusters of metal atoms and their role in the surface enhanced Raman scattering. *The Journal of Physical Chemistry* **1982**, *86* (16), 3166-3170. DOI: 10.1021/j100213a020.
(19) Scanlon, M. D.; Peljo, P.; Méndez, M. A.; Smirnov, E.; Girault, H. H. Charging and discharging at the nanoscale: Fermi level equilibration of metallic nanoparticles. *Chem. Sci.* **2015**, *6* (5), 2705-2720, 10.1039/C5SC00461F. DOI: 10.1039/C5SC00461F.
(20) Lee, D.-K.; Park, S.-I.; Lee, J. K.; Hwang, N.-M. A theoretical model for digestive ripening. *Acta Materialia* **2007**, *55* (15), 5281-5288. DOI: https://doi.org/10.1016/j.actamat.2007.05.048.
(21) Luther, J. M.; Jain, P. K.; Ewers, T.; Alivisatos, A. P. Localized surface plasmon resonances arising from free carriers in doped quantum dots. *Nature Materials* **2011**, *10* (5), 361-366. DOI: 10.1038/nmat3004.
(22) Alam, R.; Labine, M.; Karwacki, C. J.; Kamat, P. V. Modulation of Cu2–xS Nanocrystal Plasmon Resonance through Reversible Photoinduced Electron Transfer. *ACS Nano* **2016**, *10* (2), 2880-2886. DOI: 10.1021/acsnano.5b08066.
(23) Subramanian, V.; Wolf, E. E.; Kamat, P. V. Green Emission to Probe Photoinduced Charging Events in ZnO-Au Nanoparticles. Charge Distribution and Fermi-Level Equilibration. *Journal of Physical Chemistry B* **2003**, *107* (30), 7479-7485. DOI: 10.1021/jp0275037.
(24) Subramanian, V.; Wolf, E. E.; Kamat, P. V. Catalysis with TiO2/Gold Nanocomposites. Effect of Metal Particle Size on the Fermi Level Equilibration. *Journal of the American Chemical Society* **2004**, *126* (15), 4943-4950. DOI: 10.1021/ja0315199.
(25) Carroll, G. M.; Brozek, C. K.; Hartstein, K. H.; Tsui, E. Y.; Gamelin, D. R. Potentiometric Measurements of Semiconductor Nanocrystal Redox Potentials. *Journal of the American Chemical Society* **2016**, *138* (13), 4310-4313. DOI: 10.1021/jacs.6b00936.
(26) Zapata Herrera, M.; Aizpurua, J.; Kazansky, A. K.; Borisov, A. G. Plasmon Response and Electron Dynamics in Charged Metallic Nanoparticles. *Langmuir* **2016**, *32* (11), 2829-2840. DOI: 10.1021/acs.langmuir.6b00112.

(27) Mao, Z.; Espinoza, R.; Garcia, A.; Enwright, A.; Vang, H.; Nguyen, S. C. Tuning Redox Potential of Gold Nanoparticle Photocatalysts by Light. *ACS Nano* **2020**, *14* (6), 7038-7045. DOI: 10.1021/acsnano.0c01704.
(28) Haram, S. K. Semiconductor Electrodes. In *Handbook of Electrochemistry*, Zoski, C. G. Ed.; Elsevier, 2007; p 342.